A Thermodynamics Perspective on the Stepwise Conversion of Methane to Methanol over Cu-exchanged SSZ-13

Florian Göltl*[,a], Saurabh Bhandari, and Manos Mavrikakis*

Department of Chemical and Biological Engineering, University of Wisconsin - Madison, 1415 Engineering Drive, Madison, WI 53706

*corresponding authors: fgoeltl@arizona.edu, emavrikakis@wisc.edu

[a] current affiliation: The University of Arizona, Department of Biosystems Engineering, 1177 E. 4th Street, Tucson, AZ

Abstract:

Transition-metal exchanged zeolites are known to convert methane to methanol with high selectivity, in a stepwise process, involving exposure to oxidant, followed by exposure to methane, and finally by exposure to water vapor. However, a comprehensive theoretical study on the nature of the possible active sites and their respective changes during this stepwise process is still lacking. Here, we use a combination of density functional theory in its generalized-gradient approximation (DFT-GGA) calculations and post-DFT methods to identify the thermodynamically preferred sites in Cu-exchanged zeolite SSZ-13, during the stepwise conversion of methane to methanol. We develop a thermodynamic model for an extensive set of possible active sites, i.e., Cu monomers, dimers, and trimers, which are anchored in different ring structures and supported by a series of different local Al distributions. Subsequently, phase diagrams are constructed and used to identify thermodynamically favored sites, at each step during the stepwise conversion of methane to methanol. We find that during exposure to O_2, hydroxylated dimers – $Cu_2O_2H_2$ and, depending on the local Al configuration, Cu_2OH - are preferred. Upon exposure to

methane, site-bound methanol molecules are formed. With the subsequent increase in water vapor pressure a thermodynamic preference for monoatomic Cu and the release of methanol are observed. Furthermore, we compare our predicted results to experimental measurements published in the literature and find close agreement in terms of Cu coordination number and bond distances for certain of the sites considered. We expect that the insights obtained here can be used to improve our understanding of the reaction mechanism and to optimize the stepwise conversion of methane to methanol.

Keywords: Methane, Oxidation, Cu-exchanged zeolite, Density Functional Theory, Post-DFT methods, phase diagrams, Copper-oxo, Copper hydroxyl

Graphical TOC:

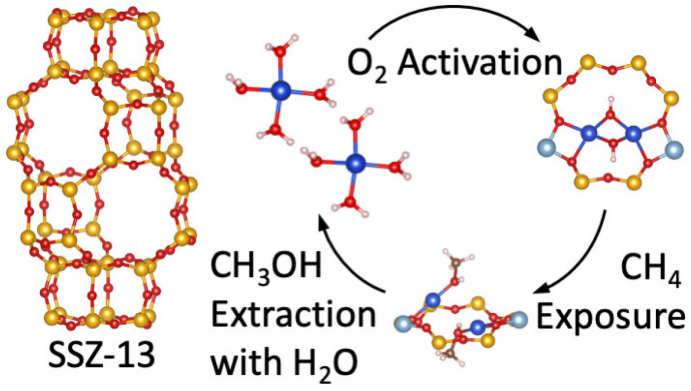

Introduction:

Selective conversion of methane to methanol has remained a major scientific and practical challenge for several decades and has attracted significant attention recently due to the increased availability of natural gas. The major challenge for this reaction is to only activate the first C-H bond in methane and prevent its over-oxidation to thermodynamically more stable CO/CO_2. Therefore, an indirect industrial process has been developed, where methane is converted to syngas[1], which is then transformed to longer chain hydrocarbons

or methanol[2,3]. The methane steam reforming conversion takes place at high temperatures and pressures and is economically not viable at remote extraction sites, where such technology could not become available. To achieve on-site conversion of methane to more valuable and easier to transport methanol, it would be desirable to find a direct route for this reaction, operated at mild conditions. In nature, this is achieved by the enzyme methane monooxygenase, where Cu- and Fe-oxo clusters serve as the active site[4–6]. Inspired by this enzymatic catalysis, extensive research has been focused on reproducing similar active sites in heterogeneous catalysts[7–9]. In particular, Cu-exchanged zeolites have drawn significant attention in this context[10–23].

Due to strict conversion/selectivity limits in the catalytic conversion of methane to methanol[24], a stepwise conversion process shows greater promise in comparison with the continuous-flow process[25]. In the stepwise process, the catalyst is activated in an oxidizing atmosphere, followed by exposure to methane. Contact of the activated catalyst with methane triggers the formation of methoxy species, which are subsequently extracted as methanol by using water vapor.

After the initial discovery of the activity of transition-metal (TM) exchanged zeolites, several oxidants[11,26–28] and zeolite structures have been tried for this reaction[17,22,26,29]. However, despite significant efforts, the nature of the active site is still under debate. This is best illustrated for Cu-exchanged Mordenite, where different studies report the presence of either Cu-oxo dimers[10,16,26,30–32] or trimers[18] as active sites for this chemistry. Further, several studies for different zeolite structures indicate a change in the active sites as a function of experimental conditions[20,30,33,34]. At the same time, full experimental characterization of a complex system like a zeolite is challenging. These difficulties are

rooted in the presence of a distribution of active sites, which show overlapping signals in Raman spectroscopy and UV-vis spectroscopy[29,35]. Even combining information with EXAFS data on coordination environments and bond distances requires a series of assumptions about the active site[33,34].

First-principles based modeling can support and extend these experimental assignments by systematically considering an extensive set of possible active site structures and by calculating their relative thermodynamic stability[36,37]. This information can then be summarized in phase diagrams, which reveal the most stable phase under various experimental conditions[38–40]. Combining the information from phase diagrams with knowledge of the anchoring point distribution, enables derivation of the site distribution present in the zeolite material under specific experimental conditions[37,41]. In the conversion of methane to methanol using Cu-exchanged zeolites, attempts so far have aimed at describing the relative stability of different Cu sites in Mordenite[42], ZSM-5[19] or SSZ-13[29,43]. These studies, however, considered only few possible active sites, which does not describe the complex distribution of sites expected to be present in such a zeolite system.

The ideal candidate zeolite-framework to study the site-speciation of Cu is SSZ-13 (Cu-SSZ-13). This is a zeolite in the Chabazite framework with a highly symmetric primitive unit cell, which limits the number of possible Cu configurations[37]. This material has been shown to efficiently convert methane to methanol[11,17,21,29,33,34] and a significant body of work on characterization of the active sites in this material already exists[29,33,34]. Lastly, Cu-SSZ-13 has been extensively studied in the context of deNO_x-SCR[44,45]. In fact, it is possible to extend the methodology developed to describe active sites during deNO_x-SCR[39] in order

to gain a comprehensive understanding of Cu-SSZ-13 in the methane to methanol conversion.

In this work, we use first-principles modeling to study the nature of the active sites in Cu-SSZ-13 during the stepwise conversion of methane to methanol. We develop a detailed theoretical model based on the chemical potential of Cu in various monomer, dimer and trimer structures in the zeolite matrix and use phase diagrams to determine the thermodynamically preferred state of Cu. We find that, depending on the local Al distribution, either $Cu_2O_2H_2$ or Cu_2OH, is stabilized during catalyst activation. When methane is introduced, methanol adsorbed to Cu monomers is formed, which desorbs when the water pressure in the system is increased. Our findings are capable of rationalizing experimental EXAFS measurements reported in the literature[33].

The stepwise conversion of methane to methanol

One of the major challenges in converting methane to methanol is to prevent methane over-oxidation to thermodynamically preferred CO_2. In catalytic conversion, selectivity/conversion limits have been derived for this chemical reaction and several strategies have been suggested to circumvent these problems[24]. For transition metal exchanged zeolites, in particular, the stepwise conversion of methane to methanol using O_2 as the oxidant has drawn significant attention[25]. The catalyst is first activated in an O_2 containing atmosphere at high temperature to generate the active sites. In a subsequent step, the system is cooled down and exposed to methane. Interaction with methane at this process step triggers the formation of surface methoxy species (i.e., oxygenates of CH_4 such as methanol), which cannot desorb. Further oxidation of methanol would require its

desorption from the Cu site, followed by regeneration of the active sites. The regeneration of the active sites would require oxidative conditions, but since oxygen is absent during methane exposure, no further active sites are formed, and stably adsorbed surface methoxy species are protected from overoxidation. In a final step, methanol is extracted at lower temperature by introducing water vapor to the system.

For the studies reported in the literature, the fundamental steps remain similar, i.e., activation is followed by methane exposure and methanol extraction. However, the exact experimental conditions can vary between different research groups, which can influence methanol yields[22]. For Cu-SSZ-13, a systematic analysis of the impact of various experimental parameters on the performance of each step in this process has been reported in the literature[33]. Here, we will focus on conditions described as optimal for Cu-SSZ-13 by Pappas et al. (see Fig. 1), which are as follows:

1 Initial exposure to 1 bar O_2 at 323 K;

2 Ramping the temperature to 773 K, under 1 bar O_2;

3 Stopping the O_2 flow at 773 K;

4 Cooling the system to 473 K and initiate exposure to 1 bar of CH_4;

5 Stopping the CH_4 flow at 473 K;

6 Exposure to 0.1 bar of H_2O at 473 K;

Typically, at points 1, 3 and 5, conditions change abruptly (see Fig. 1), while the system is kept at specific conditions for several hours for points 2, 4, and 6 (see Fig. 1). At some points of the process (e.g., after 3, 4, and 5), the system is exposed to inert gases (such as He) to remove excess gas pressures from previous exposure. Inert gases do not influence site speciation and are, therefore, omitted from further discussion below.

While the externally applied gas pressures are known, residual pressures of the other gases, caused by impurities in the supplied gases or small amounts of gases adsorbed in the zeolite nanopores from previous exposure, will also be present. The exact values will depend on the experimental setup and the detailed process protocol. However, since residual gas pressures are impossible to measure experimentally, we use approximate values for them. If not explicitly stated otherwise, we assume a logarithmic O_2 gas pressure $\ln(P^{O_2}/P_0)$=-7, a logarithmic H_2O gas phase pressure $\ln(P^{H_2O}/P_0)$=-7 and after exposure to CH_4, a residual logarithmic CH_4 pressure $\ln(P^{CH_4}/P_0)$=-9. All pressures are calculated with respect to a reference pressure P_0 of 1 bar. The list of all parameters at each point along the stepwise conversion process for methane to methanol is given in Supporting Information, Table S1. Careful testing revealed that the choice of residual pressures has only a subtle effect on results. Wherever variation of the residual pressures affects the results, we explicitly discuss them.

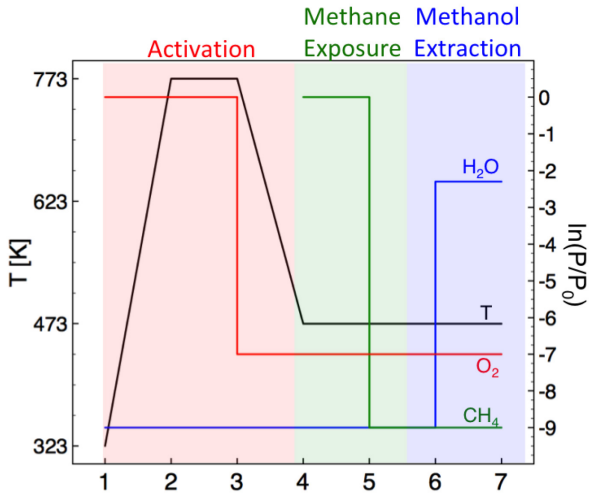

Figure 1: A representation of the conditions during the stepwise conversion of methane to methanol. Temperature (black line) is given in Kelvin and gas-phase pressure of various participating species (red, green, and blue lines) are given as natural logarithms with respect to a reference pressure P_0 of 1 bar. The temperature and partial pressure profiles of various components correspond to the left and right y-axis, respectively. Shaded regions correspond to catalyst activation (red), methane exposure (green) and methanol extraction (blue), respectively.

Methods:

The Thermodynamic Model:

Structures included in the model: We focus on the Cu exchanged zeolite SSZ-13. SSZ-13 is a material with the chabazite structure, the zeolite framework structure with the smallest primitive unit cell. This feature reduces the complexity of the system, while still retaining all basic features associated with zeolites, which makes this material a nearly ideal test-system for zeolite catalysis. The framework is composed of corner-sharing SiO_4 tetrahedral (T-sites), which form a double six O-ring (6R) building block, containing 12 T-sites representing one-unit cell (see Fig. 2 (a)). The unit cells are connected by four O-rings, which leads to a medium-sized pore and the formation of eight O-rings (8R) (see Fig. 2 (c)). The framework is chemically functionalized by replacing Si by Al in some of the T-sites. Compared to Si, Al has one less valence electron and cannot saturate all bonds to the surrounding O atoms. This electron-deficiency is compensated for by the presence of positively charged ions. Most commonly, these are Brønsted protons, but since we are interested in Cu-exchanged zeolites, we choose Cu (monomers) and Cu-clusters (dimers and trimers), which are formed after Cu ion exchange, as compensating ions.

The distribution of Al atoms is controlled during synthesis, but throughout this work, we assume that, similar to defects in solids, a distribution of local Al configurations exists in the zeolite[36,46]. The exact distribution of local Al configurations will most likely vary

between different zeolite samples. Typically for this chemistry, SSZ-13 samples in medium to high Si/Al ratio range (>8), have been found to be the most promising in terms of methanol yield per Cu atom[17]. We, therefore, model unit cells containing one (Si/Al=11) and two (Si/Al=5) Al atoms, which, under the assumption of good Al dispersion, most likely represent the majority of the local Al configurations present in SSZ-13 zeolites used in the literature. Additionally, we assume that the Loewenstein rule is valid[47], i.e., Al-O-Al bonds are not allowed, and include all possible, symmetrically different Al configurations in the primitive unit cell. This leads to one Al configuration for the 1Al case and five different Al configurations for the 2Al case (2Al-A through 2Al-E)[48], all of which are shown in Fig. 2b.

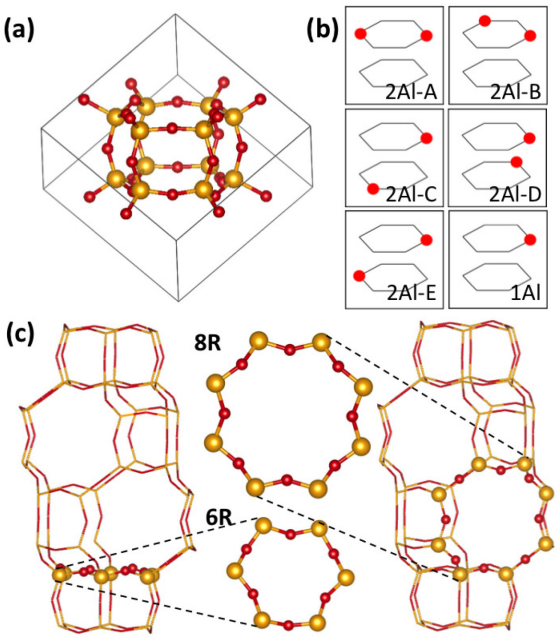

Figure 2: (a): The primitive unit cell of the purely siliceous SSZ-13 framework. (b): Schematic representation of the various local Al configurations for Cu_1 exchange studied in a single unit cell. Si(Al)-O-Si bonds in the six O-rings are shown as black lines, Al positions are marked by red circles. (c): Extended structure of purely siliceous SSZ-13 zeolite, with potential Cu_1 exchange positions in the six O-ring (6R) and eight O-ring (8R) highlighted. Highlighted structures displayed using a ball and stick model, while the remaining framework is displayed using a stick representation, are linked to framework models using dashed lines. In the atomistic representation,

Si is shown as yellow spheres and O as red spheres. Atomistic structures in (c) are displayed without Al or Cu. Al atoms replace Si atoms as shown in the schematic representation in (b). Cu atoms are either located in the 6R or 8R structure, with the lowest energy structures dependent on the positioning of the Al atoms and the coordinated H_2O molecule(s).

To study Cu speciation within the SSZ-13 zeolite framework, we consider an extensive set of plausible Cu sites. We start our discussion with mononuclear Cu (Cu_1) sites included in our model, which have been extensively discussed in the literature[36,38,39,49–51], followed by the Cu-dimer and Cu-trimer sites.

In zeolites, Cu_1 can exist in two different oxidation states, namely Cu_1(I) and Cu_1(II), which require one and two compensating charges, respectively. Scheme 1 shows several ways to generate Cu_1(I) and Cu_1(II). When only one Al atom is close to the Cu atom, as is the case for the 1Al configuration, one electron is transferred from Cu to the Al-O bonds and Cu_1(I) will be formed (see Scheme 1 (a)). When two Al atoms are present close to the Cu atom, as is the case in 2Al-A through 2Al-E, Cu_1(I) will require the presence of a proton to compensate for the second negative charge (see Scheme 1 (b)). If the proton is not present, Cu_1(II) will be formed (see Scheme 1 (c)). Additionally, it is possible to form Cu_1(II), if a water molecule is split to form Cu_1(II)-OH and a proton adsorbed to an O atom adjacent to the second Al atom (see Scheme 1 (d)). Similarly, Cu_1(II)-OH bound to the 1Al configuration forms Cu_1(II) (see Scheme 1 (e)).

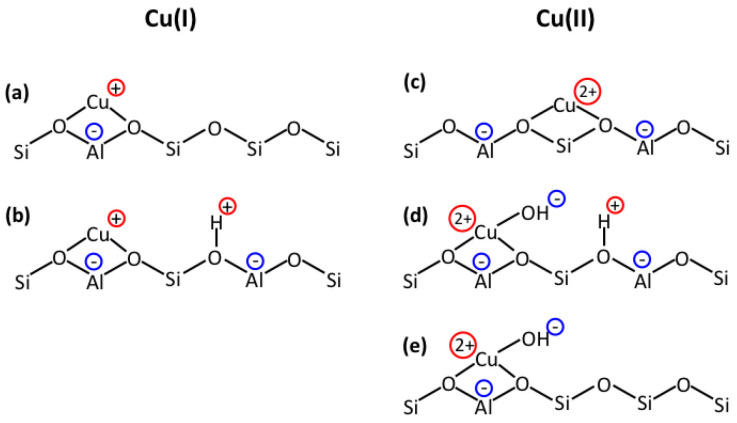

Scheme 1: Schematic representation of different ways to generate Cu_1(I) and Cu_1(II) in zeolites. For Cu_1(I) one uncompensated charge needs to be present, for Cu_1(II) two uncompensated charges are required. Cu_1(I) can either be generated by adding Cu to a 1Al unit cell (a) or by adding a proton and a Cu atom to a 2Al unit cell (b). Cu_1(II) can be generated by adding a Cu atom to a 2Al unit cell (c), by adding Cu-OH and a proton to a 2Al unit cell (d) or Cu-OH to a 1Al unit cell (e). In schematic representations black lines show bonds, blue circles represent negative charges and red circles represent positive charges. All structural files for sites included in our model are provided in Supporting Information (Cu_1(I)) and the Supporting Information of reference 32.

Cu_1 species can be stabilized in the 6R or the 8R (exchange sites are shown in Fig. 2 (c)). During the stepwise conversion of methane to methanol, the zeolite is exposed to a series of different gas-phase environments. It has been reported that, in particular, the presence of H_2O changes Cu coordination and leads to Cu-H_2O complexes at lower temperatures[38,39]. We, therefore, explore all the different possibilities to form Cu_1(I) and Cu_1(II) located in a 6R and 8R, for all Al configurations shown in Fig. 2 (b), and allow for the coordination of Cu_1 with up to six H_2O molecules, which will allow for the formation of Cu_1-hexaaqua species. A detailed discussion of all Cu_1(II) has been given in the literature and we rely on the related published structures[39]. For Cu_1(I), we follow a similar strategy, and all the optimized structure files are provided in the Supporting Information. Only the most stable Cu_1(I) and Cu_1(II) structures for a given number of adsorbed H_2O molecules are included in our thermodynamic model. In subsequent phase diagrams, these structures

are labeled as: Cu(I)+nH_2O and Cu(II)+nH_2O for Cu_1(I) and Cu_1(II) sites, respectively, with n adsorbed H_2O molecules each.

In the literature, several different Cu dimers and trimers have been suggested to be active in the conversion of methane to methanol[18,26,29,42]. Similar to the Cu_1 case, Cu in dimers and trimers will bind to O atoms adjacent to framework Al, but these structures are generally too large to fit into the double 6R structure of a unit cell. We, therefore, constructed four different local Al configurations reaching over adjacent unit cells, two of which are located in the same 8R (see D-A and D-B in Fig. 3 (a) and 8R in Fig. 3 (b))[29,35]. The other two Al configurations allow for Cu dimers bridging a 6R and an adjacent 8R (D-C and D-D in Fig. 3 (a) and 6R/8R Fig. 3 (b)). We construct $Cu_2O_yH_z$ (y=1, 2; z≤y) dimers, for all four Al configurations (D-A though D-D). For the $Cu_2O_2H_2$ stoichiometry we furthermore considered the formation of associated monomers, which have been suggested as active sites for methane to methanol conversion in Mordenite[52] and Zeolite Omega[53]. Additionally, the presence of Cu trimers bound in 8R structures has been suggested for Mordenite[18]. We, therefore, include $Cu_3O_3H_z$ (z≤3) clusters for the D-A and D-B Al configurations. Accordingly, and herein, the different clusters are denoted by X-$Cu_xO_yH_z$, where X stands for A through D, which denotes Al configurations D-A through D-D, while x, y and z describe the cluster stoichiometry.

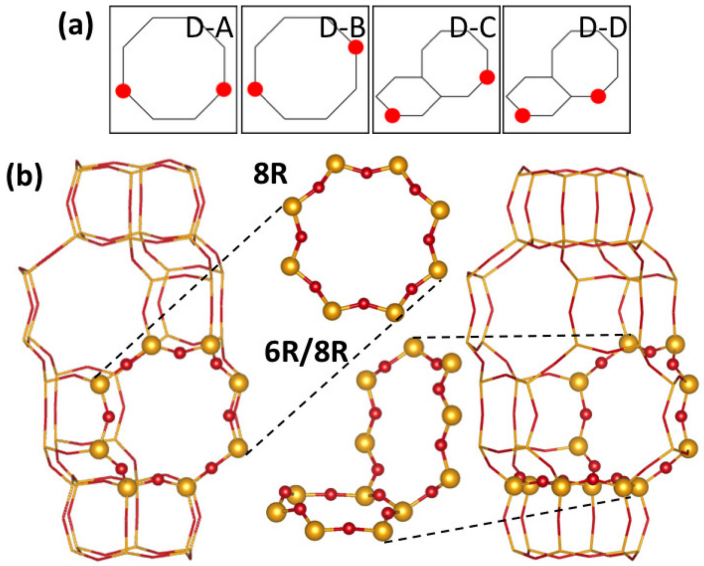

Figure 3: (a) Schematic representation of local Al configurations for dimer/trimer anchoring. Si(Al)-O-Si bonds are shown as black lines, the Al positions are marked by red circles. (b) Extended structure of SSZ-13 zeolite, with highlighted dimer exchange sites in the eight O-ring (8R) and bridging a six O-ring and an eight O-ring (6R/8R). Highlighted structures, displayed using a ball and stick model, while the remaining framework is displayed using a stick representation, are linked to framework models using dashed lines. In the atomistic representation, Si is shown as yellow spheres and O as red spheres.

All structures were optimized using the PBE-TS[54,55] density functional and periodic boundary conditions as implemented in VASP[56,57]. Several spin states were probed for each configuration. The spin ground state is used for further analysis and relative energies for the different spin states are given in Supporting Information, section S2. All optimized structures are shown in Fig. 4; structural files are provided in Supporting Information.

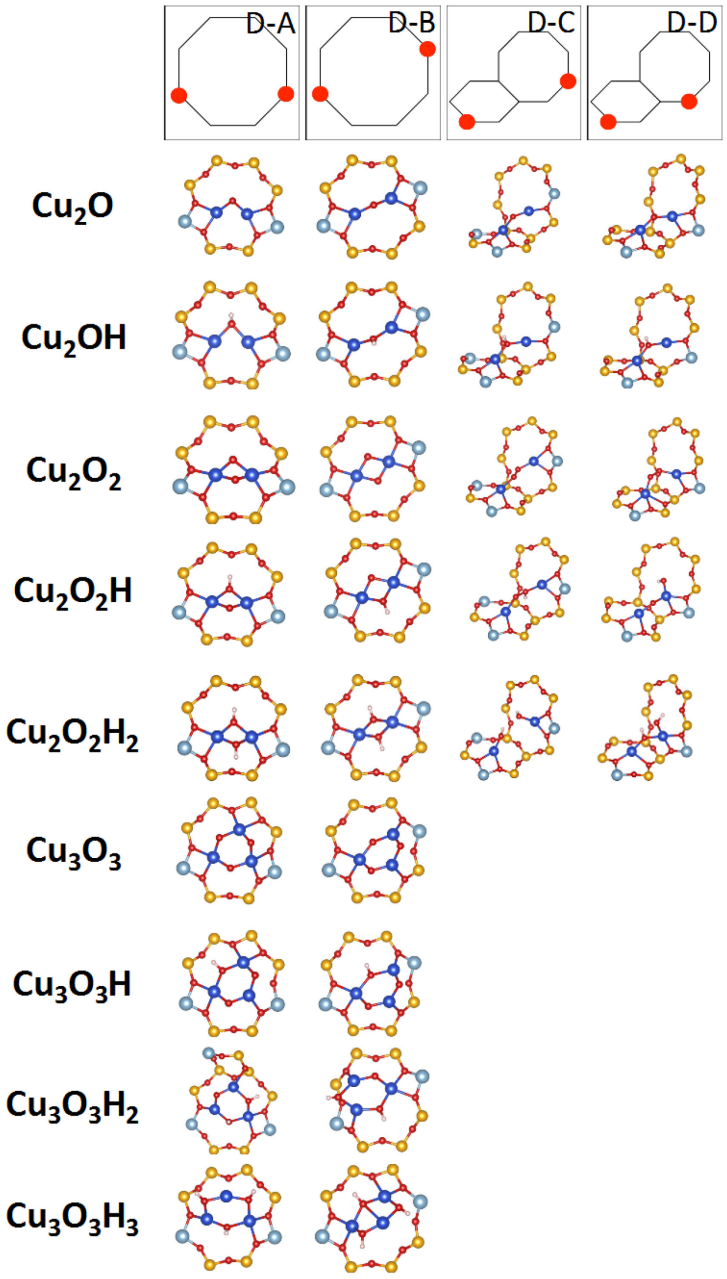

Figure 4: A graphical representation of Cu dimer and Cu trimer structures included in the thermodynamic model developed here. At the very top the Al configuration for the studied exchange sites is shown and on the left column the studied stoichiometries are given. Atomistic pictures show the optimized structures. In these pictures red atoms correspond to O, yellow atoms to Si, blue atoms to Cu, white atoms to H and blue-grey atoms to Al. As described in the caption of Fig. 2 and Fig. 3, in the schematic representations (very top of the figure) black lines show Si-O-Si bonds and red circles indicate the position of Al. All structures are included in Supporting Information. The presence of a third Al atom in atomistic structures of Al configuration D-C is an artifact of the periodic boundary conditions chosen in this work. A detailed discussion is given in Supporting Information, section S3. All structural files for sites included in our model are provided in Supporting Information.

Model construction:

In our thermodynamic model, we assume that - due to the long activation and reaction times - the system reaches its thermodynamic equilibrium during each step. We, therefore, rely on the thermodynamically most stable of all considered configurations and neglect potential intermediate states of the system. Whenever necessary, we will explicitly discuss cases where intermediate states might be important to understand the performance of Cu-SSZ-13 in the stepwise conversion of methane to methanol.

To develop a thermodynamic model, we rely on structures obtained from static structural optimization using PBE-TS[54,55]. While functionals using the generalized gradient approximation are known to lead to reasonable structural guesses (i.e. systematic errors of ~1-2% in terms of bond length[58]), comparison with post Hartree Fock/post DFT methods such as MP2[59] or the Adiabatic-Connection Fluctuation-Dissipation Theorem in its Random Phase Approximation (RPA)[60], shows significant errors for reaction energies in the deprotonation of isobutene in ZSM-5 and in the conversion of methane to methanol over Fe-oxo sites in SSZ-13[61,62]. Furthermore, RPA has shown excellent performance in describing the adsorption of alkanes in protonated zeolites[63,64]. We, therefore, use RPA to calculate total energies for each PBE-TS optimized configuration. To derive the finite temperature Gibbs Free Energies reported here, we incorporate vibrational zero point energies, and entropic corrections from static vibrational corrections calculated using the PBE-TS functional[39].

Since a Cu-SSZ-13 particle is not connected to an external Cu reservoir, we assume that after ion exchange, the number of Cu atoms in the zeolite matrix is constant. At any point in time, a distribution of Cu sites is present in the material and the total energy of the system

is the sum over the energies of all Cu atoms and every time a Cu atom changes its coordination environment and moves from one type of active site to another, the total energy of the system changes. Additionally, only a modest increase in methanol yield with activation time[33] indicates that Cu cations move quickly in the zeolite matrix compared to the time-scales typically associated with the various steps in the experimental procedure. Therefore, Cu will always be present as the configuration in its thermodynamically preferred position with the lowest chemical potential μ^{Cu} (i.e., the lowest energy per Cu atom). Since we are interested in a reaction environment containing O_2 and H_2O, we calculate μ^{Cu} for sites anchored in unit cells containing 2Al as

$$\mu^{Cu}_{Cu_xO_yH_z}(T, P^{O_2}, P^{H_2O}) =$$

$$\frac{G^{Cu_xO_yH_z-zeo}(T) - G^{2H-zeo}(T) - \frac{2y-z+2}{4}\mu^{O_2}(T, P^{O_2}) - \frac{z-2}{2}\mu^{H_2O}(T, P^{H_2O})}{x}$$

where, G indicates the Gibbs free energy of the structure in the superscript, where $Cu_xO_yH_z$-zeo indicates $Cu_xO_yH_z$ bound to the zeolite framework and 2H-zeo refers to a zeolite framework passivated by Brønsted protons. The gas phase chemical potentials of O_2 (μ^{O_2}) and H_2O (μ^{H_2O}) are obtained by correcting the energies obtained from static electronic structure PBE-TS calculations using vibrational zero-point corrections, translational, vibrational and rotational entropies, and pressures. When only one Al atom is present in the unit cell (for the 1Al Cu_1 case), the formula for μ^{Cu} is

$$\mu^{Cu}_{Cu_1O_yH_z}(T, P^{O_2}, P^{H_2O}) =$$

$$G^{Cu_1O_yH_z-zeo}(T) - G^{H-zeo}(T) - \frac{2y-z+1}{4}\mu^{O_2}(T, P^{O_2}) - \frac{z-1}{2}\mu^{H_2O}(T, P^{H_2O}) .$$

Throughout this work, we will use μ^{Cu} to calculate phase diagrams. In a realistic zeolite system, Cu will occupy the most stable Al configuration and as soon as it is filled, the next

most stable Al configuration will be occupied[36,39,65], which we account for in our study. The exact nature of the observed Cu species will therefore depend on the distribution of local Al configurations, which is expected to vary based on the synthesis and material parameters across the zeolite samples[66].

Here, we systematically study the impact of the Al distribution on the observed Cu sites. More specifically, to identify the thermodynamically preferred states for Cu in the zeolite framework, we focus on the influence of two parameters on the phase diagram: (i) the availability of anchoring points for dimers/trimers (D-A through D-D shown in Fig. 3 (a)) and (ii) the availability of the anchoring points for Cu_1 sites (1Al, 2Al-A through 2Al-E shown in Fig. 2 (b)). We calculate the phase diagrams for each of the dimer/trimer Al configuration (four possibilities) with every specific monomer Al configuration (six possibilities), which leads to a total of 24 phase diagrams for each set of conditions. This systematic approach enables insights into the relative stability of Cu at these Al configurations and into the nature of the active sites as a function of available Al configurations. In the main text, we discuss phase diagrams for all Cu dimer/trimer anchoring sites and Cu_1 monomers in 1Al (the only possible 1Al configuration) and 2Al-A (the most stable 2Al configuration[39]). Phase diagrams for Cu_1 in Al configurations 2Al-B through 2Al-E are presented in Supporting Information. Furthermore, a detailed legend to the phase diagrams presented here is given in Figure 5. Throughout the manuscript, we explicitly mention if other combinations of dimer/trimer Al configurations or monomer Al configurations are used.

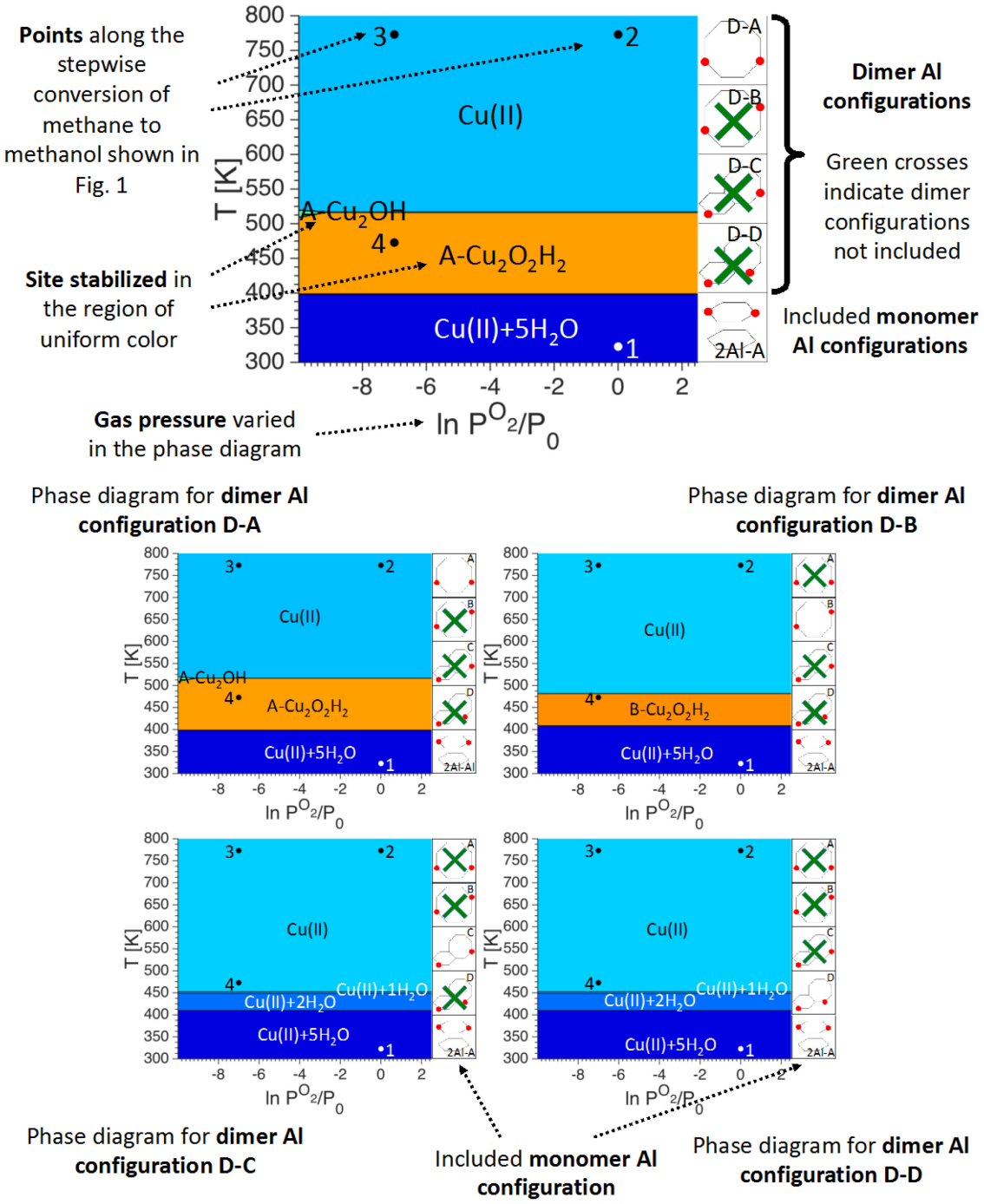

Figure 5: Detailed legend for the phase diagrams shown in Figures 6, 9 and 10 in the main text and Figures S2, S3, S4, S6 and S7 in Supporting Information. At the top the legend for each individual phase diagram is shown and at the bottom the arrangement of panels in Figures 6, 9, 10, S2, S6 and S7 is given.

Computational Methods:

All calculations were performed using the Vienna Ab-Initio Simulation Package (VASP)[56,57], a plane wave code using PAW pseudo potentials[67], adapted by Joubert and Kresse[68]. All calculations were performed with an energy cut-off for plane waves of 420 eV and were restricted to the Γ-point. The basic unit cell parameters for periodic calculations are given in the literature[69] and the zeolite volume was set to 830 $Å^3$. As described in the main text, all structures were optimized using Density Functional Theory in the parameterization of Perdew, Burke and Ernzerhof[54]. van der Waals interactions were introduced using the Tkatchenko-Scheffler force field[55]. Prior to optimization a 5 ps molecular dynamics simulation at 500 K using the Andersen thermostat[70] was performed and three different structures obtained after equal simulation times from the last 1 ps of this simulation were optimized. In all calculations the spin-states of the different clusters remained fixed and the spin-state leading to the lowest energy was used for further analysis. All minimum spin states are given in Supporting Information, section S2. For these spin states RPA calculations were performed[60,62]. Here the energy cut-off was increased to 600 eV and the energy cut-off for the response function was set to 250 eV. RPA calculations were restricted to the spin ground state determined in DFT calculations. In a subsequent step, harmonic vibrational frequencies were calculated at the PBE-TS level by numerical differentiation of the forces using a second-order finite difference approach with a step size of 0.01 Å. Vibrational and translational entropies as well as zero point vibrational corrections for gas phase molecules and zeolite unit cells were calculated using the code thermo.pl[71], a code provided by the National Institute of Standards and Technology. The impact of including translational entropies for the zeolite unit cells on μ^{Cu}, the chemical

potential of Cu, is discussed in the supporting Information, section S3. To remove unphysical translational modes and low energy vibrational modes, only vibrational frequencies above 50 cm^{-1} were considered in the analysis. For computational efficiency we reproduced dimer configurations D-A through D-D, which reach over two adjacent double six O-ring structures, in a single unit cell using periodic boundary conditions. To confirm the validity of this approach, we compared energies for dimers in the Al configuration D-C for a single and double primitive unit cell and found that energies per Cu atom calculated at the PBE-TS level lie within 6 kJ/mol (see Supporting Information, section S3). Such small energy differences indicate that constructing dimer and trimer structures in a single primitive unit cell is a good approximation. Gas phase molecules were modeled in a 10 Å x 10.1 Å x 12 Å box.

Zeolite Activation

Phase diagrams:

The first step in the stepwise conversion of methane to methanol is the activation of the catalyst through its exposure to the oxidant for generating the active sites. Here two variables play a crucial role, namely the O_2 pressure (P^{O_2}) and temperature (T). The T/P^{O_2} phase diagrams are presented in Fig. 6 (for Cu_1 in (a) 1Al and (b) 2Al-A) and Fig. S2 (for Cu_1 in 2Al-B through 2Al-E). A detailed legend to these figures is given in Fig. 5. We start the analysis by including dimer configurations D-A through D-D, one at a time, with Cu_1 bound to the 1Al configuration (Fig. 6 (a)). It is interesting to observe that for Al configurations D-A and D-B, mainly Cu_2OH and $Cu_2O_2H_2$ are found to be stable. At D-A, A-$Cu_2O_2H_2$ is found to be stable at low temperatures, while A-Cu_2OH is stable at higher

temperatures. For configuration D-B, B-$Cu_2O_2H_2$ is almost exclusively preferred. For Al configurations D-C and D-D, which bridge the 6R and 8R, only Cu_2OH is found as dimer site. At lower temperatures, Cu_1(I) with one or two adsorbed H_2O molecules is stabilized. Next, we repeat the procedure described above considering the scenario where Cu_1 binds to the 2Al-A configuration, instead of the 1Al configuration, and find that the results are quite different (see Fig 6 (b)). While the $Cu_2O_2H_2$ sites are still stabilized in a narrow temperature range for Al configurations D-A and D-B, phase diagrams are otherwise dominated by monoatomic Cu_1(II). At higher temperatures, the Cu atom is located in the 6R, while at lower temperatures Cu_1(II) is coordinated to up to five H_2O molecules. The dominance of Cu_1(II) at higher temperatures is intimately linked to its stability in the 6R[36,39]. When Cu_1 binds to 2Al-B through 2Al-E (see Fig. S2 (a)-(d) in Supporting Information), trends in between the extreme cases of least stable Cu_1 in 1Al and most stable Cu_1 in 2Al-A are observed. At low temperatures, hydrated Cu_1(II) sites are found to be stable. Dehydrated, monoatomic Cu_1(II), on the other hand, is only stabilized for 2Al-B (Fig. S2 (a)) and 2Al-D (Fig. S2 (c)) in a small region in the phase diagram at high T and P^{O_2}. At the same time, Cu dimers are stabilized in a relatively large T/P^{O_2} range.

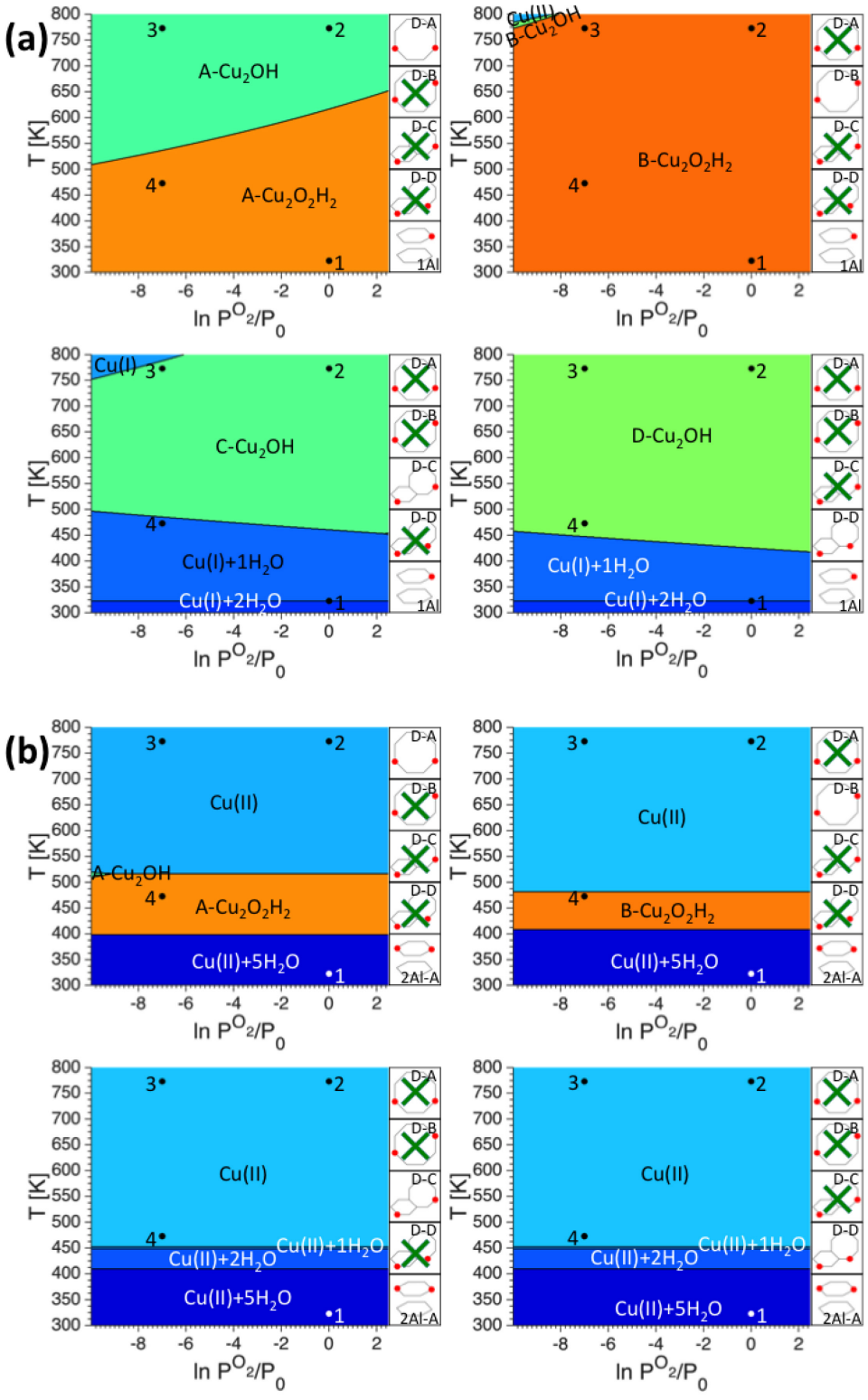

Figure 6: Zeolite Activation through exposure to O_2: T/$\mathbf{P^{O_2}}$ phase diagrams for different Al configurations for dimer/trimer anchoring and (a) Cu_1 anchored in a 1Al configuration or (b) the 2Al-A configuration. The temperature is given in Kelvin (K) and $\mathbf{P^{O_2}}$ is given with respect to a reference pressure of one bar. The thermodynamically preferred sites are indicated by regions of

identical color and the site type is indicated by the labels. The included Al configurations are indicated by schematic representations on the right side of the phase diagrams, which correspond to Fig. 2 (b) and Fig. 3 (a). Green crosses indicate Al configurations not included in the phase diagrams. Points marked with numerals: 1, 2, 3, and 4, correspond to specific points in the stepwise methane to methanol conversion, as defined in Fig. 1. A detailed legend is given in Fig. 5.

So far, we have studied phase diagrams where only one possible dimer/trimer Al configuration and one monomer configuration was included. However, in a realistic system, multiple Al configurations will be available. Here, initially Al configurations leading to most stable $Cu_xO_yH_z$ species will be occupied. While extensive discussion about relative stability of Cu_1 in SSZ-13 exists in the literature[36,38,39,48,65], the relative stability of dimers has been discussed on a limited basis. We, therefore, study phase diagrams including all four Al configurations for dimer formation (D-A through D-D) and Cu_1 bonded to the 1Al configuration (see Fig. S3) and find that A-Cu_2OH and A-$Cu_2O_2H_2$ are the most stable Cu dimers (Fig. S3) when all dimer exchange sites are available. In a realistic system, only a finite number of Al configurations D-A will exist, therefore, after they are filled with dimers, the next most stable sites will be formed[37]. We remove Al configuration D-A from the phase diagrams and find that B-$Cu_2O_2H_2$ is the second most stable site at low T/high P^{O_2}, while D-Cu_2OH is most stable at high T/low P^{O_2}. When removing either D-B or D-D we find that the other site becomes dominant, which indicates that C-Cu_2OH is the least stable dimer structure and will therefore be formed last.

Using these phase diagrams, we can follow the sites during the first four steps of the stepwise conversion (see Fig. 1, Fig. 6, and Fig. S2). Initially, the system is at 323 K under O_2 pressure of 1 bar (point 1 in Fig. 1). For all 2Al configurations (Fig. 6 (b) and Fig. S2 (a)-(d)), Cu is found as Cu_1(II) and is coordinated to five or six H_2O molecules. For Cu_1 in 1Al (see Fig. 6 (a)), Cu forms $Cu_2O_2H_2$ if the D-A or D-B configuration is available or it

is present as Cu_1(I) coordinated to one or two H_2O molecules otherwise. Subsequently, the system is heated to 773 K (point 2 in Fig. 1) and now in almost all cases dimers are formed. For Al configurations D-A, D-C, and D-D the preferred configuration is Cu_2OH, while for D-B, $Cu_2O_2H_2$ is preferred. For Cu_1 anchored in Al configuration 2Al-A (Fig. 6 (b)) and 2Al-D (Fig. S2 (c) in Supporting Information), however, Cu_1(II) located in the six-ring is found to be stable. In a following step O_2 flow is stopped and P^{O_2} is reduced to e^{-7} (point 3 in Fig. 1). This reduction in pressure leaves most of the sites unchanged, only if 2Al-D (Fig. S2 (c)) is included for Cu_1 formation, Cu dimers are now preferred over Cu_1(II). In step four (point 4 in Fig. 1), the system is cooled to 473 K and at this point for Al configurations D-A and D-B, $Cu_2O_2H_2$ is always preferred. For Al configurations D-C and D-D, the situation is somewhat more complex. For these two dimer exchange sites Cu_1 in several 2Al configurations (2Al-A (Fig. 6 (b)), 2Al-B, 2Al-C and in part 2Al-D (Fig. S2 (a)-(c)) is preferred over dimer formation. However, we cannot exclude that dimer decomposition is slow, compared to the reaction times, and therefore dimers might initially still be present at these conditions.

It is interesting to see that at an activation temperature of 773 K several local Al configurations lead to the formation of Cu_1(II). The activation temperature for zeolites has been a topic of discussion[11,22,33]. To accelerate dimer formation the highest possible temperature that still allows for ideal performance is preferred. However, at some temperature, monomer formation becomes thermodynamically favorable. Typically, an upper limit of 723 K is assumed, but Pappas et al. report an increase in methanol production at 773 K[33]. In our analysis at this temperature, the formation of monomers was preferred for two of the 2Al configurations (2Al-A (Fig. 6 (b) and 2Al-D (Fig. S2 (c)). However, we

relied on a residual O_2 pressure (P^{H_2O}) of e^{-9}. When studying the P^{H_2O} dependence during activation for Al configuration D-A and Cu_1 in 2Al-A (see Fig. S4), we find that an increase in P^{H_2O} shifts the transition to Cu_1(II) to higher temperatures, i.e., a slightly higher P^{H_2O} will allow for higher activation temperatures during dimer formation.

Comparison to experimental data:

The nature of the active sites in Cu-SSZ-13 during catalyst activation has been studied in detail using *in situ* EXAFS measurements[33], and the following qualitative observations were made: (i) a minority of Cu sites do not form dimers during the activation process and (ii) the coordination number of a fraction of Cu atoms increases from three to four when Cu-SSZ-13 is activated in O_2 at 773 K and 473 K. As we will show in the following, both observations are well reproduced from the phase diagrams constructed here. Fig. 6 (b) and Fig. S2 (c) show that monoatomic Cu_1 in the 2Al-A and 2Al-D configurations is more stable than dimers or trimers at high T and high P^{O_2}. Therefore, Cu_1 in the 2Al-A and 2Al-D configurations will not form dimers during the high temperature activation process, which in agreement with the experimental observations. Furthermore, for Al configuration D-A, threefold coordinated Cu in the dimer A-Cu_2OH will be formed at 773 K, but fourfold coordinated Cu in A-$Cu_2O_2H_2$ will be most stable for activation at 473 K. Cu in the next most stable dimers B-$Cu_2O_2H_2$ and D-Cu_2OH will not change its coordination number. Therefore, for activation at 773 K, Cu hosted in dimers in Al configuration D-A will be in a three-fold coordinated structure, while after activation at 473 K, Cu in Al configuration D-A will be in a four-fold coordinated structure, which agrees perfectly with experimental observations documenting an increase in Cu coordination number at lower activation temperatures.

EXAFS measurements containing information about the coordination shells of Cu and distinct coordination peaks at distances of 1.86±0.05 Å, 1.97±0.04 Å, 2.72±0.02 Å and 3.41 Å have been observed[33]. To reproduce these values, we studied the structural information of all the dimers and compare them to experimentally measured values (Fig. 7). We split the information into distances between Cu-O in the dimer, Cu-O in the framework, Cu-Cu and Cu-Al atoms. We find that distances between Cu and the O atom for hydroxyl groups in the dimers, correspond (within error) to 1.86 Å, while the experimentally measured distance of 1.97 Å corresponds to the distances between Cu and O atoms in the zeolite framework. The 2.72 Å distance can either be attributed to one of the: Cu-Al distances, the Cu-Cu distance in A-$Cu_2O_2H_2$, or, with larger error, to the Cu-Cu distances in B-$Cu_2O_2H_2$ and A-Cu_2OH. The Cu-Cu distances for B-Cu_2OH, C-Cu_2OH and D-Cu_2OH, on the other hand agree well with the experimentally observed distance at 3.41 Å. We emphasize the excellent agreement between model sites we predicted and experimental EXAFS measurements. In particular, with the most stable A-$Cu_2O_2H_2$ with a Cu-OH distances of 1.91 Å and 1.92 Å (experiment 1.86±0.05 Å), Cu and O atoms in the zeolite framework of 1.97 Å and 2.04 Å (experiment 1.97±0.04 Å), Cu-Al distances of 2.72 Å and 2.74 Å and a Cu-Cu distance of 2.73 Å (experiment 2.72±0.02 Å). Thus, we find excellent agreement between experimental measurements and the sites predicted to be stable based on our phase diagrams.

While structural agreement between the stable sites and experiment is encouraging, the presence of other sites such as CuOH, Cu_2O_2, Cu_2O, or Cu trimers, which have been previously suggested in the literature to be the active sites in the methane to methanol conversion[10,16,18,29,72], is still possible. We therefore discuss bond-lengths for these sites in

Supporting Information section S7 and show that the presence of such sites in Cu-SSZ-13 after activation is unlikely.

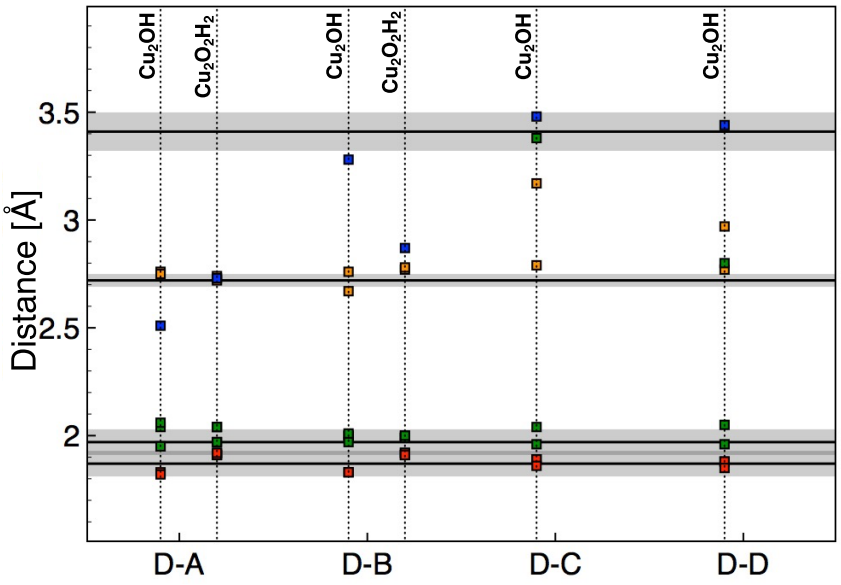

Figure 7: Bond distances calculated for sites predicted to be stable in Cu-SSZ-13. Red symbols indicate distances between Cu and O in the Cu-dimers, green symbols distances between Cu and O in the framework, yellow denotes Cu-Al distances and blue symbols show Cu-Cu distances. X-axis labels correspond to the local Al configurations. Dashed vertical lines mark the following sites for each Al configurations (from left to right) Cu_2OH (D-A through D-D) and $Cu_2O_2H_2$ (D-A and D-B) (see Fig. 4). Black horizontal lines indicate literature values for bond distances measured using EXAFS[33] and grey shaded areas mark the experimentally reported error bars.

Methane activation

After the activating the zeolite by exposure to an oxidant, the zeolite is exposed to methane to form methanol adsorbed on Cu sites. To determine the nature of the material under these conditions, we model the adsorbed methanol molecules in the zeolite framework. To keep the discussion tractable, we focus on methanol formation at the most stable sites during the activation step of the entire process, namely A-$Cu_2O_2H_2$ and B-$Cu_2O_2H_2$ and all Cu_2OH sites. In the following, we assume that each OH group can form one methanol molecule and substitute the OH groups by methanol. To balance the stoichiometries, excess H atoms are included as water molecules in the mathematical description below. A recombination with oxygen could happen by e.g. H diffusing to the zeolite framework[28]. For Cu_2OH we

model the adsorption of one methanol molecule and for $Cu_2O_2H_2$ we model all possibilities for the adsorption of one methanol molecule (the other OH group remains intact) or two methanol molecules. The most stable structures for a given stoichiometry are displayed in Fig. 8. For Cu_2OH in configurations D-C and D-D, and for $Cu_2O_2H_2$ dimers in configuration D-A and D-B, formation of methanol leads to the decomposition of the dimer and leaves methanol adsorbed to Cu_1(I). For the adsorption of a single methanol molecule to $Cu_2O_2H_2$, a Cu_2OH dimer remains intact, and one methanol molecule is adsorbed to one of the Cu centers, while a dimer containing a methanol molecule is formed for Cu_2OH in Al configurations D-A and D-B.

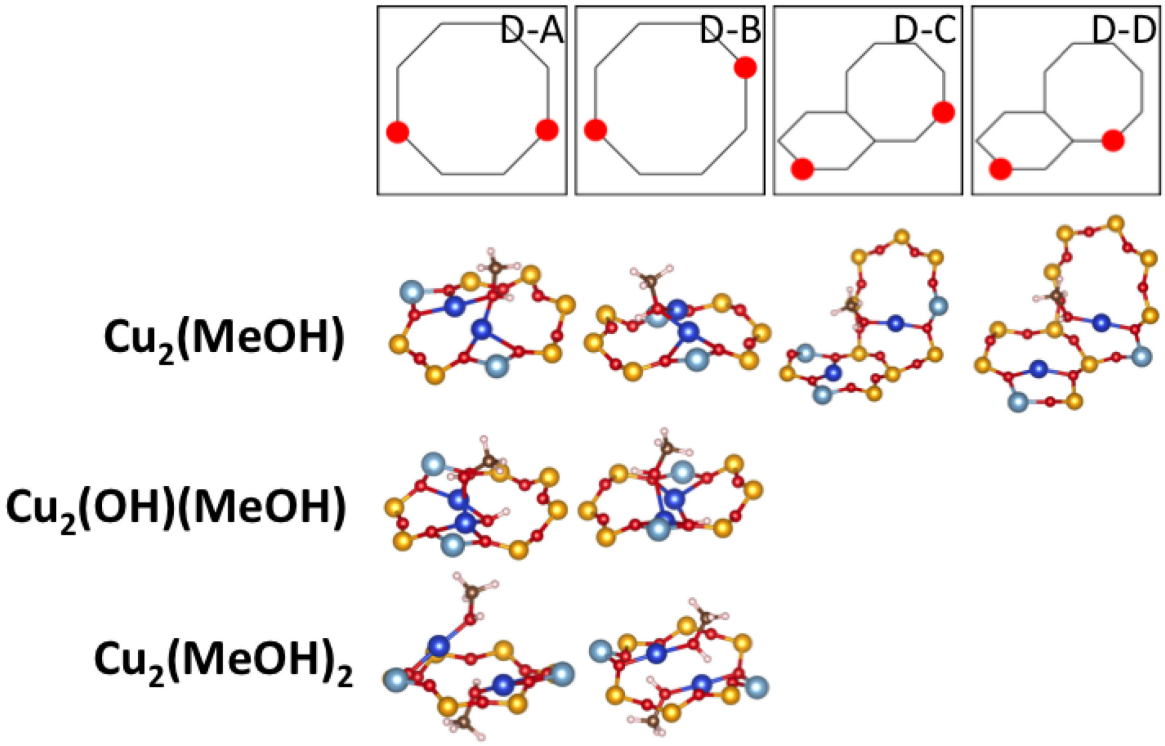

Figure 8: A graphical representation of all stable sites after exposure to methane and formation of methanol (MeOH). At the top of the figure, the different local Al configurations of the exchange sites are given (see Fig. 3 (a)) and on the left the stoichiometries of the different Cu site structures are listed. The color code corresponds to Fig. 4; C atoms are displayed in brown. MeOH is used as shorthand notation for methanol. All structural files for sites included in our model are provided in Supporting Information

Similar to the definition provided earlier, we calculate μ^{Cu} for unit cells containing two Al atoms and adsorbed methanol molecules as

$$\mu^{Cu}_{Cu_xO_yH_z(CH_3)_w}(T, P^{O_2}, P^{H_2O}, P^{CH_4}) =$$

$$\frac{G^{Cu_xO_yH_z-zeo}(T) - G^{2H-zeo}(T) - w\mu^{CH_4}(T,P^{CH_4}) - \frac{2y-z+2+w}{4}\mu^{O_2}(T,P^{O_2}) - \frac{z-w-2}{2}\mu^{H_2O}(T,P^{H_2O})}{x},$$

where, definitions provided earlier are extended here by *w*, the number of CH_3 groups in the system, P^{CH_4}, the CH_4 pressure and μ^{CH_4}, the chemical potential of CH_4 in gas phase. Using this definition, it is possible to perform an analysis similar to the one performed for the zeolite activation phase during exposure to oxidant.

Similar to the discussion for activation above, we use μ^{Cu} to study the stability of Cu sites with adsorbed methanol molecules. Again, we discuss all possible combinations of dimer exchange sites D-A through D-D and monomer exchange sites (1Al and 2Al-A through 2Al-E). As a first step, we analyze T/P^{CH_4} phase diagrams (see Fig. 9 and Fig. S6 in Supporting Information; a detailed legend for these figures is given in Fig. 5). In general, we find that the phase diagrams for Al configurations D-A and D-B are dominated by methanol containing structures. For Al configurations D-A and D-B at high pressures, the formation of two methanol molecules is preferred. For Al configuration D-A, the formation of a Cu_2OH dimer with methanol binding to one of the Cu atoms is thermodynamically favored at low P^{CH_4}. For D-C and D-D, a structure containing two Cu atoms and one methanol molecule is favorable. Only at high temperatures and low methanol pressures the initial dimers are kept intact and methane is not converted to methanol. When varying the anchoring of Cu_1, a picture similar to the zeolite activation conditions emerges. For 1Al Cu_1 is preferred only for Al configurations D-C and D-D at low T and P^{CH_4} (see Fig. 9 (a)).

For the 2Al-A on the other hand, Cu_I is far more stable and prohibits the formation of methanol for Al configurations D-C and D-D for most of the condition space (see Fig. 9 (b)). The other 2Al configurations lie between these extremes (see Fig. S6 (a)-(d) in Supporting Information). Similar to Cu_I anchored in 1Al (see Fig. 9 (a)), for Cu_I in most of the 2Al configurations the formation of one or two methanol molecules is preferred for Cu in dimer Al configurations D-A and D-B (see Fig. 9 (b) and Fig. S6 (a)-(d)). For D-C and D-D, on the other hand, a significant portion of the phase diagram is dominated by Cu_I. For 2Al-B (Fig. S6 (a)) and to a lesser extent 2Al-C (Fig. S6 (b)) this leads to a preference for Cu_I at reaction temperatures, while for 2Al-D (Fig. S6 (c)) and 2Al-E (Fig. S6 (d)) methanol formation is favorable.

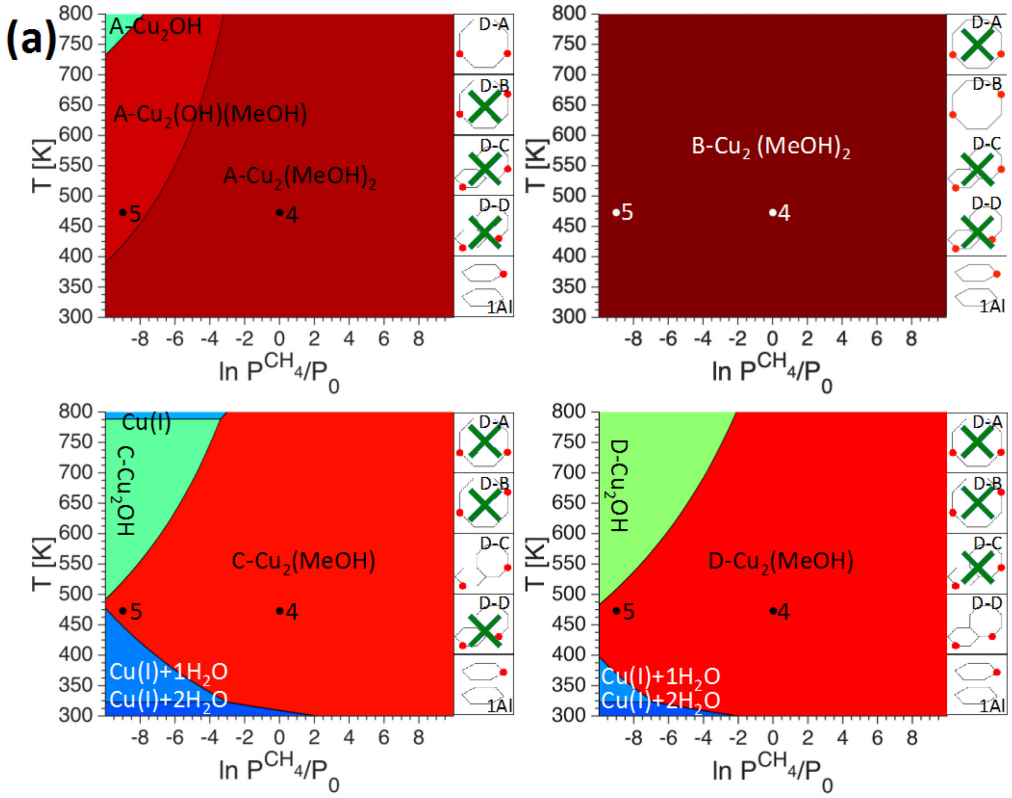

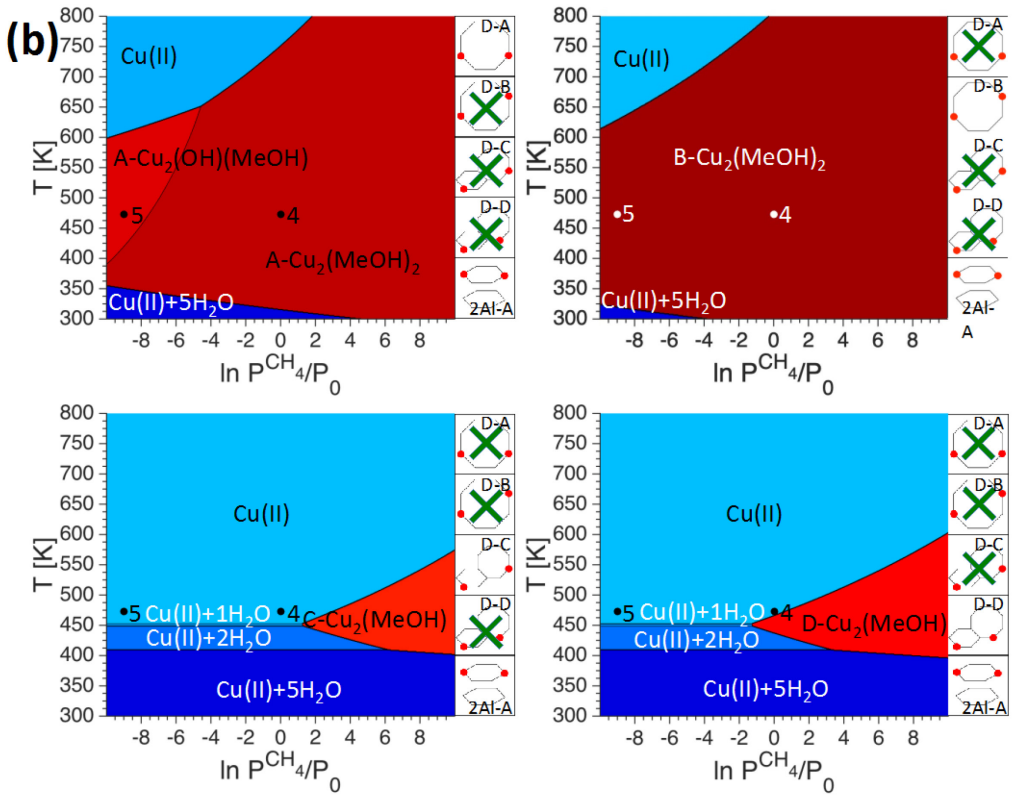

Figure 9: Activated zeolite exposed to CH_4: T/$\mathbf{P^{CH_4}}$ phase diagrams for different Al configurations for dimer/trimer anchoring and (a) Cu_I anchored in a 1Al configuration or (b) the 2Al-A configuration. Temperature is given in K and $\mathbf{P^{CH_4}}$ is given with respect to a reference pressure of one bar. Regions of identical color indicate the thermodynamically preferred sites; the site type is indicated by the labels. The included Al configurations are indicated by schematic representations on the right side of the phase diagrams, which correspond to Fig 2 (b) and Fig 3 (a). Green crosses indicate Al configurations not included in the phase diagrams. Points marked with 4 and 5 correspond to labels in Fig. 1. A detailed legend is given in Fig. 5.

Methanol extraction

The last step in the stepwise conversion of methane to methanol is the extraction of methanol by introducing water vapor to the system (see Fig. 1). Accordingly, we focus on a T/P^{H_2O} phase diagram in the presence of methanol (see Fig. 10, Fig. S7 in Supporting Information; a detailed legend for these figures is given in Fig. 5). We find that for Cu_I in the 2Al configurations (see Fig. 10 (b) and Fig S7 (a)-(d)) an increase in P^{H_2O} leads to the

preference of Cu_I for D-A and D-B and, therefore, methanol will desorb. For Al configurations D-A and D-B and Cu_I in 1Al methanol adsorbed to Cu remains stable until higher P^{H_2O}. For Al configurations D-C and D-D methanol is only found when Cu_I is located in the 1Al, 2Al-D and 2Al-E configurations. This is consistent with the T/P^{CH_4} phase diagrams (see Fig. 9 and Fig. S6), where adsorbed methanol was not stabilized for the corresponding Al configurations.

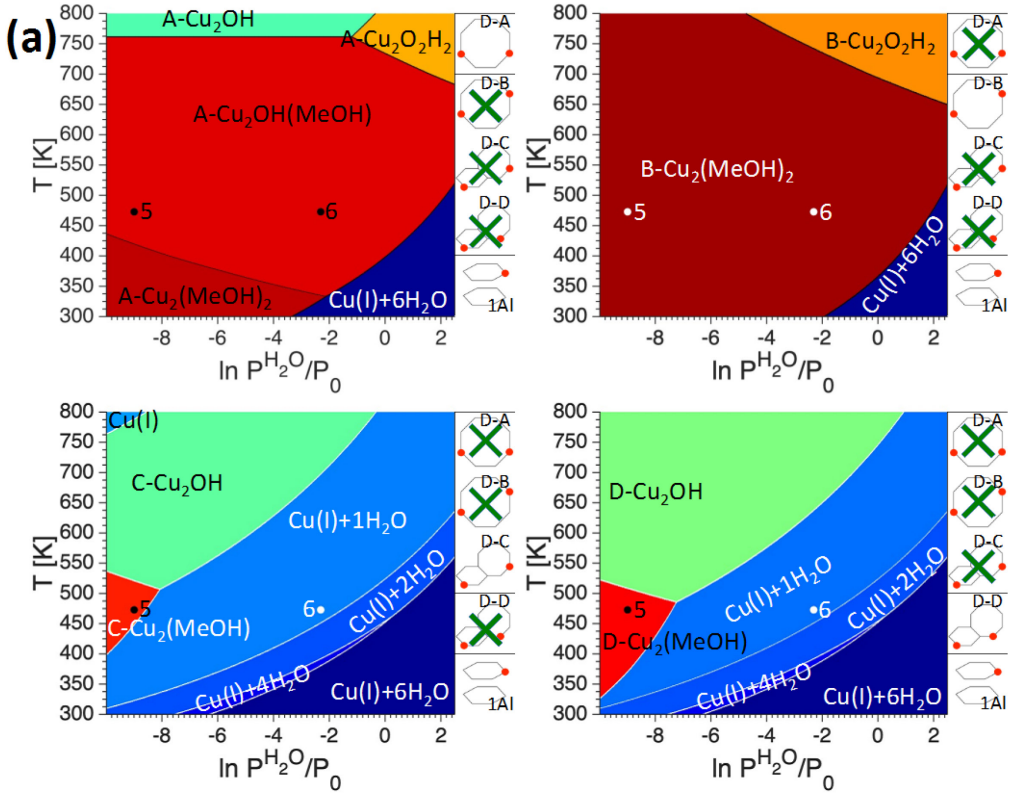

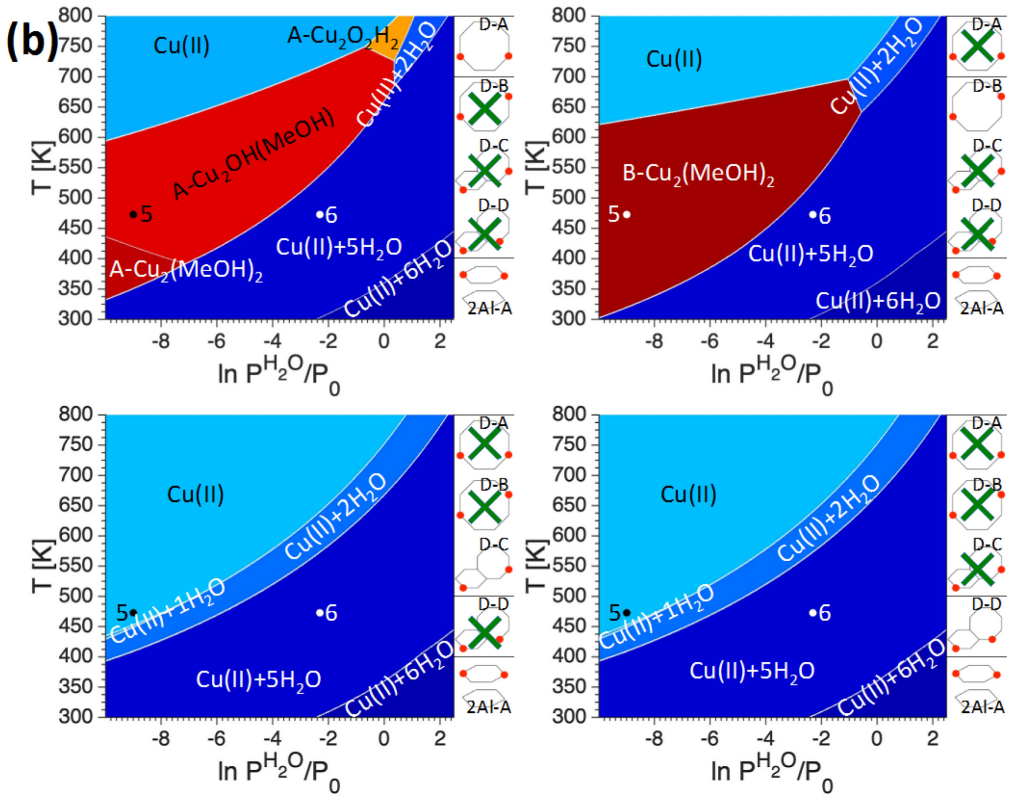

Figure 10: Methanol extraction by exposure to water vapor: T/$\mathbf{P^{H_2O}}$ phase diagrams for different Al configurations for dimer/trimer anchoring and (a) Cu monomers anchored in a 1Al configuration or (b) the 2Al-A configuration in the presence of CH_4. Temperature is given in K and $\mathbf{P^{H_2O}}$ is given with respect to a reference pressure of one bar. The thermodynamically preferred sites are indicated by regions of identical color; the site type is indicated by the labels. The included Al configurations are indicated by schematic representations on the right side of the phase diagrams, which correspond to Fig. 2 (b) and Fig. 3 (a). Green crosses indicate Al configurations not included in the phase diagrams. Points marked with 5 and 6 correspond to labels in Fig. 1. A detailed legend is given in Fig. 5.

It is now possible to follow the nature of the active sites through methane activation and methanol extraction. After the introduction of methane at 1 bar almost all sites start to form adsorbed methanol molecules (see Fig. 9 and Fig. S6). Only for C-Cu_2OH and D-Cu_2OH sites and the most stable Cu_I in 2Al-A and 2Al-B no methanol is formed, which might be associated with the absence of hydroxylated dimers during activation in the first place (see Fig. 6 (b) and Fig S2 (a)). When P^{CH_4} is reduced, in some cases methanol is directly released. For Al configurations D-A and D-B and for Cu_I in 2Al-A (see Fig. 10 (b)) an

increase in P^{H_2O} to 0.1 bar leads to the release of methanol. For perfectly separated Al atoms, as represented by 1Al (see Fig. 10 (a)), methanol remains stable and cannot be extracted. For Cu_1 in the other 2Al configurations (2Al-B through 2Al-E, see Fig. S7 (a)-(d)) a transition between Cu_1 bonded to methanol and Cu_1 coordinated to water is right at P^{H_2O}=0.1 bar. For these sites potentially a slightly lower temperature (e.g., 408 K) during H_2O treatment would make methanol release more likely.

Discussion:

As discussed earlier, the methodology presented here almost perfectly reproduces experimentally measured bond lengths and coordination numbers reported in the experimental literature[73]. However, contrary to common interpretations the thermodynamic model developed here reveals that hydroxylated dimers ($Cu_2O_2H_2$ or Cu_2OH) are most stable and most likely the sites active in this reaction. In particular, Cu-O bond lengths from EXAFS measurements agree perfectly with the Cu-O distances in the most stable $Cu_2O_2H_2$, whereas the oxo sites Cu_2O and Cu_2O_2 and Cu-OH underestimate Cu-O distances by about 10%. At the same time, various parameters, such as the Al distribution and the encountered conditions might determine the exact dimer stoichiometry and geometry. While our model is focused on SSZ-13, many zeolite frameworks with ring structures similar to the chabazite framework exist. In these zeolite frameworks, similar Cu exchange sites exist, and similar Cu site structures might be stabilized. For other zeolite frameworks the anchoring point geometry varies significantly, which might lead to different preferred active site structures. Thus, a systematic study, similar to that presented here, would be required on other zeolitic frameworks to determine the effect of structural

properties on the plausible Cu sites. However, based on the clear thermodynamic trends for Cu-SSZ-13, we hypothesize that in different zeolite structures, where other monomer and dimer exchange sites exist, and different local Al configurations will be present, a similar preference for hydroxylated Cu structures might occur when O_2 is used as an oxidant.

The presence of hydroxylated dimers raises significant questions relevant to methane activation. Methane activation over oxo-sites has been extensively discussed and is often proposed to proceed via an abstraction and rebound step[74,75] or a concerted mechanism[76]. In zeolites only Cu-OH has been discussed as a potential hydroxylated active site[72]. However, the site geometries presented in this work imply different mechanisms (see Scheme 2) and based on our results we hypothesize the following: For $Cu_2(OH)$ stoichiometric arguments point towards H_2 formation during the activation of CH_4 (Scheme 2 (a)). Indeed, experimental measurements indicate the formation of small quantities of H_2 during methane exposure[28,33]. On the other hand, for the $Cu_2O_2H_2$ sites a similar mechanism activating two CH_4 molecules and forming two methanol molecules is possible (see Scheme 2 (b)-(i)). This mechanism leads to thermodynamically preferred structures for D-A and D-B (see Fig. 9 and Fig. S6 in Supporting Information). For such a mechanism formation of H_2 is necessary, which might require to overcome significant activation energy barriers. Accordingly, accurate measurements of the molar ratios of H_2 to methanol produced during methane exposure could support this reaction mechanism.

At the same time, a simpler mechanism is possible for $Cu_2O_2H_2$ sites (see Scheme 2 (b)-(ii)): Methane gets activated at one OH group and the abstracted H atom combines with the other OH on the site to form water, while the methyl group forms methanol with the

first OH group on the site. This mechanism, would therefore, after the desorption of H_2O, favor the formation of Cu_2(MeOH), which is not always found to be most stable in the phase diagrams presented in Fig. 9, Fig. 10, Fig. S6, and Fig. S7, but might be the only site accessible after methane activation. Such a mechanism (Scheme 2 (b)-(ii)) is supported by the highest methanol yields per Cu atom reported in the literature, which is limited to ~0.5 methanol/Cu atom[31], i.e. the production of one methanol per Cu-dimer.

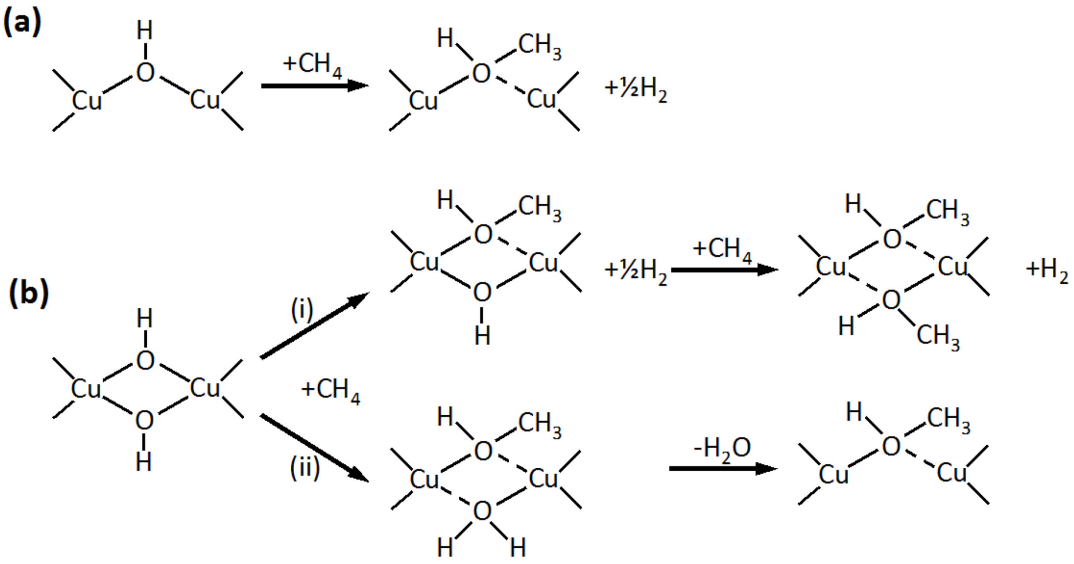

Scheme 2: Suggested reaction pathways for the activation of methane over (a) Cu_2OH and (b) $Cu_2O_2H_2$ sites. For (a) and (b)-(i), methane gets activated at the OH group and methanol is formed. Excess H diffuses away from the Cu active site[28] and recombines as H_2. For (b)-(ii) methane forms methanol and H_2O at one $Cu_2O_2H_2$ site. Strong chemical bonds are displayed as black lines, dashed lines represent weak bonds (~2.5 Å or longer) that, depending on the exact active site geometry, can be easily broken. Open ended bonds at Cu represent bonds to zeolite framework O atoms.

One of the most surprising observations made in this work is that at no point Cu-OH, a site that is believed to be active in the selective catalytic reduction of NO_x[38,45] and has been suggested to be active in the conversion of methane to methanol[72], is stabilized. It remains to be seen whether the presence of NH_3, as encountered in deNO_x-SCR, can stabilize Cu-OH over hydroxylated Cu-dimers.

Conclusions

We have explored the nature of the most stable Cu sites in zeolite SSZ-13 during the stepwise conversion of methane to methanol, using O_2 as the oxidant. We generated a model that includes a series of different Cu dimers and trimers, as well as hydrated Cu_1(I) and Cu_1(II) sites, stabilized in different local Al configurations. We used a combination of DFT and post-DFT calculations to construct phase diagrams and determine the nature of the most stable sites during: catalyst activation, methane exposure and methanol extraction. The most stable site at each point in the stepwise conversion of methane to methanol is shown in Scheme 3. We find that in the initial catalyst activation phase, depending on the local Al configurations and the exact conditions, $Cu_2O_2H_2$ or Cu_2OH dimers are formed. When methane is introduced to the system, methanol molecules bound to Cu sites in the zeolite are generated. Finally, an increase in the water pressure leads to MeOH desorption. We closely compare the prediction from our thermodynamic model to experimental measurements[33] in the literature and find excellent agreement.

1	2	3	4 (no CH_4)	4 (CH_4)	5	6
	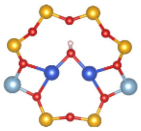	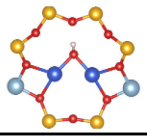	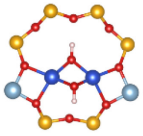	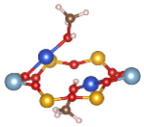	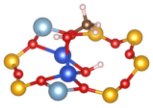	
Cu_1(II)+5H2O*	A-Cu_2OH	A-Cu_2OH	A-$Cu_2O_2H_2$	A-$Cu_2(MeOH)_2$	A-$Cu_2OHMeOH$	Cu_1(II)+5H_2O*
Initial State	Activation			Methane Exposure		Methanol Extraction

Scheme 3: Schematic representation of the most stable Cu sites at each point along the stepwise conversion of methane to methanol in SSZ-13. The labels at the top line of the scheme correspond to the points shown in Fig. 1. For points 2 through 5, the most stable Cu sites anchored in the D-A configuration is displayed. At points 1 and 6, the structure most often encountered for all monomer anchoring sites is shown. For point 4, two possibilities were considered, one without CH_4 (labeled as: no CH_4) and one in the presence of CH_4 (labeled as: CH_4). Color code: red circles denote O,

yellow Si, blue Cu, white H and blue-grey Al, respectively. *At 1 and 6, all H_2O molecules not directly coordinated to Cu are omitted for clarity.

In particular, the prediction that hydroxylated dimers are thermodynamically preferred and at no point Cu-oxo sites, such as Cu_2O, Cu_2O_2, or Cu_3O_3, are stable, contradicts common assumptions about the nature of active Cu centers in zeolites and also enzymes active in the conversion of methane to methanol. In the future, it will be interesting to see to what extent our findings can be utilized to arrive at an improved understanding of this reaction and how we may be able to optimize the conditions for the stepwise process of methane to methanol conversion.

Supporting Information: Supporting Information contains information about the studied reaction conditions along the stepwise conversion of methane to methanol, the preferred spin states for Cu dimers and trimers, the effect of translational entropy, the effect of unit cell size, a graphical legend to the phase diagrams and phase diagrams for Al configurations 2Al-B through 2Al-E. Furthermore, phase diagrams for the relative stability of dimers in the different exchange sites is given. Additionally, all dimer/trimer/Cu_1(I) structure files are provided.

Acknowledgements: This work was supported by the National Science Foundation, grant number CHE-1800284. We thank Dr. Roberto Schimmenti and Dr. Tibor Szilvasi for careful editing of the manuscript. We thank Dr. Ambarish Kulkarni (UC Davis) for his suggestions during the review process. We acknowledge computational time at the National Energy Research Scientific Computing Center (NERSC), a DOE Office of

Science User Facility supported by the Office of Science of the U.S. Department of Energy, contract DE-AC02-05CH11231. This research was in part performed using the computing resources and assistance of the UW-Madison Center for High Throughput Computing (CHTC) in the Department of Computer Sciences. The CHTC is supported by UW-Madison, the Advanced Computing Initiative, the Wisconsin Alumni Research Foundation, and the Wisconsin Institutes for Discovery, and the National Science Foundation, and is an active member of the Open Science Grid, which is supported by the National Science Foundation and the U.S. Department of Energy's Office of Science.

References:

(1) Da Silva, M. J. Synthesis of Methanol from Methane: Challenges and Advances on the Multi-Step (Syngas) and One-Step Routes (DMTM). *Fuel Process. Technol.* **2016**, *145*, 42–61.

(2) Khodakov, A. Y.; Chu, W.; Fongarland, P. Advances in the Development of Novel Cobalt Fischer−Tropsch Catalysts for Synthesis of Long-Chain Hydrocarbons and Clean Fuels. *Chem. Rev.* **2007**, *107* (5), 1692–1744.

(3) Grabow, L. C.; Mavrikakis, M. Mechanism of Methanol Synthesis on Cu through CO 2 and CO Hydrogenation. *ACS Catal.* **2011**, *1*, 365–384.

(4) Lieberman, R. L.; Rosenzweig, A. C. Crystal Structure of a Membrane-Bound Metalloenzyme That Catalyses the Biological Oxidation of Methane. *Nature* **2005**, *434* (7030), 177–182.

(5) Balasubramanian, R.; Smith, S. M.; Rawat, S.; Yatsunyk, L. A.; Stemmler, T. L.; Rosenzweig, A. C. Oxidation of Methane by a Biological Dicopper Centre. *Nature* **2010**, *465* (7294), 115–119.

(6) Shu, L.; Nesheim, J. C.; Kauffmann, K.; Münck, E.; Lipscomb, J. D.; Que, L. An Fe2 IV O2 Diamond Core Structure. *Science (80-.).* **1997**, *275*, 515–518.

(7) Nauert, S. L.; Rosen, A. S.; Kim, H.; Snurr, R. Q.; Stair, P. C.; Notestein, J. M. Evidence for Copper Dimers in Low-Loaded CuO_x / SiO_2 Catalysts for Cyclohexane Oxidative Dehydrogenation. *ACS Catal.* **2018**, *8*, 9775–9789.

(8) Rosen, A. S.; Notestein, J. M.; Snurr, R. Q. Structure–Activity Relationships That Identify Metal–Organic Framework Catalysts for Methane Activation. *ACS Catal.* **2019**, *9*, 3576–3587.

(9) Doan, H. A.; Li, Z.; Farha, O. K.; Hupp, J. T.; Snurr, R. Q. Theoretical Insights into Direct Methane to Methanol Conversion over Supported Dicopper Oxo Nanoclusters. *Catal. Today* **2018**, *312*, 2–9.

(10) Woertink, J. S.; Smeets, P. J.; Groothaert, M. H.; Vance, M. A.; Sels, B. F.; Schoonheydt, R. A.; Solomon, E. I. A $[Cu_2O]^{2+}$ Core in Cu-ZSM-5 , the Active

Site in the Oxidation of Methane to Methanol. *Proc. Natl. Acad. Sci.* **2009**, *106*, 18908–18913.
(11) Ipek, B.; Lobo, R. F. Catalytic Conversion of Methane to Methanol on Cu-SSZ-13 Using N_2O as Oxidant. *Chem. Commun.* **2016**, *5* (300), 1668–1686.
(12) Mahyuddin, M. H.; Staykov, A.; Shiota, Y.; Yoshizawa, K. Direct Conversion of Methane to Methanol by Metal-Exchanged ZSM-5 Zeolite (Metal = Fe, Co, Ni, Cu). *ACS Catal.* **2016**, *6* (12), 8321–8331.
(13) Mahyuddin, M. H.; Tanaka, T.; Staykov, A.; Shiota, Y.; Yoshizawa, K. Dioxygen Activation on Cu-MOR Zeolite: Theoretical Insights into the Formation of Cu_2O and Cu_3O_3 Active Species. *Inorg. Chem.* **2018**, *57* (16), 10146–10152.
(14) Mahyuddin, M. H.; Shiota, Y.; Yoshizawa, K. Methane Selective Oxidation to Methanol by Metal-Exchanged Zeolites: A Review of Active Sites and Their Reactivity. *Catal. Sci. Technol.* **2019**, *9* (8), 1744–1768.
(15) `Mahyuddin, M. H.; Tanaka, T.; Shiota, Y.; Staykov, A.; Yoshizawa, K. Methane Partial Oxidation over $[Cu_2(\mu\text{-}O)]^{2+}$ and [Cu3(μ-$O)_3$]2+ Active Species in Large-Pore Zeolites. *ACS Catal.* **2018**, *8* (2), 1500–1509.
(16) Vanelderen, P.; Snyder, B. E. R.; Tsai, M.-L.; Hadt, R. G.; Vancauwenbergh, J.; Coussens, O.; Schoonheydt, R. A.; Sels, B. F.; Solomon, E. I. Spectroscopic Definition of the Copper Active Sites in Mordenite : Selective Methane Oxidation. *J. Am. Chem. Soc.* **2015**, *137* (19), 6383–6392.
(17) Wulfers, M. J.; Lobo, R. F.; Ipek, B.; Teketel, S. Conversion of Methane to Methanol on Copper-Containing Small-Pore Zeolites and Zeotypes. *Chem. Commun.* **2015**, *51* (21), 4447–4450.
(18) Grundner, S.; Markovits, M. A. C.; Li, G.; Tromp, M.; Pidko, E. A.; Hensen, E. J. M.; Jentys, A.; Sanchez-Sanchez, M.; Lercher, J. A. Single-Site Trinuclear Copper Oxygen Clusters in Mordenite for Selective Conversion of Methane to Methanol. *Nat. Commun.* **2015**, *6*, 7546.
(19) Li, G.; Vassilev, P.; Sanchez-Sanchez, M.; Lercher, J. A.; Hensen, E. J. M.; Pidko, E. A. Stability and Reactivity of Copper Oxo-Clusters in ZSM-5 Zeolite for Selective Methane Oxidation to Methanol. *J. Catal.* **2016**, *338*, 305–312.
(20) Le, H. V.; Parishan, S.; Sagaltchik, A.; Goebel, C.; Schlesiger, C.; Malzer, W.; Trunschke, A.; Schomaecker, R.; Thomas, A. Solid-State Ion-Exchanged Cu/Mordenite Catalysts for the Direct Conversion of Methane to Methanol. *ACS Catal.* **2017**, *7*, 1403–1412.
(21) Narsimhan, K.; Iyoki, K.; Dinh, K.; Román-Leshkov, Y. Catalytic Oxidation of Methane into Methanol over Copper-Exchanged Zeolites with Oxygen at Low Temperature. *ACS Cent. Sci.* **2016**, *2* (6), 424–429.
(22) Sushkevich, V. L.; Bokhoven, J. A. Van. Methane-to-Methanol : Activity Descriptors in Copper-Exchanged Zeolites for the Rational Design of Materials. *ACS Catal.* **2019**, *9*, 6293–6304.
(23) Mahyuddin, M. H.; Staykov, A.; Shiota, Y.; Miyanishi, M.; Yoshizawa, K. Roles of Zeolite Confinement and Cu-O-Cu Angle on the Direct Conversion of Methane to Methanol by $[Cu_2(\mu\text{-}O)]_{2+}$-Exchanged AEI, CHA, AFX, and MFI Zeolites. *ACS Catal.* **2017**, *7* (6), 3741–3751.
(24) Latimer, A. A.; Kakekhani, A.; Kulkarni, A. R.; Nørskov, J. K. Direct Methane to Methanol: The Selectivity-Conversion Limit and Design Strategies. *ACS Catal.*

2018, *8* (8), 6894–6907.
(25) Ravi, M.; Sushkevich, V. L.; Knorpp, A. J.; Newton, M. A.; Palagin, D.; Pinar, A. B.; Ranocchiari, M.; Bokhoven, J. A. Van. Misconceptions and Chellenges in Methane-to-Methanol over Transition-Metal-Exchanged Zeolites. *Nat. Catal.* **2019**, *2*, 485–494.
(26) Groothaert, M. H.; Smeets, P. J.; Sels, B. F.; Jacobs, P. A.; Schoonheydt, R. A. Selective Oxidation of Methane by the Bis(μ-Oxo)Dicopper Core Stabilized on ZSM-5 and Mordenite Zeolites. *J. Am. Chem. Soc.* **2005**, *127* (5), 1394–1395.
(27) Hammond, C.; Forde, M. M.; Ab Rahim, M. H.; Thetford, A.; He, Q.; Jenkins, R. L.; Dimitratos, N.; Lopez-Sanchez, J. A.; Dummer, N. F.; Murphy, D. M.; et al. Direct Catalytic Conversion of Methane to Methanol in an Aqueous Medium by Using Copper-Promoted Fe-ZSM-5. *Angew. Chemie - Int. Ed.* **2012**, *51* (21), 5129–5133.
(28) Sushkevich, V. L.; Palagin, D.; Ranocchiari, M.; Bokhoven, J. A. Van. Selective Anaerobic Oxidation of Methane Enables Direct Synthesis of Methanol. *Science (80-.).* **2017**, *356*, 523–527.
(29) Ipek, B.; Wulfers, M. J.; Kim, H.; Göltl, F.; Hermans, I.; Smith, J. P.; Booksh, K. S.; Brown, C. M.; Lobo, R. F. Formation of $[Cu_2O_2]^{2+}$ and $[Cu_2O]^{2+}$ toward C-H Bond Activation in Cu-SSZ-13 and Cu-SSZ-39. *ACS Catal.* **2017**, *7* (7), 4291–4303.
(30) Pappas, D. K.; Martini, A.; Dyballa, M.; Kvande, K.; Teketel, S.; Lomachenko, K. A.; Baran, R.; Glatzel, P.; Arstad, B.; Berlier, G.; et al. The Nuclearity of the Active Site for Methane to Methanol Conversion in Cu-Mordenite : A Quantitative Assessment. *J. Am. Chem. Soc.* **2018**, *140*, 15270–15278.
(31) Dyballa, M.; Pappas, D. K.; Kvande, K.; Borfecchia, E.; Arstad, B.; Beato, P.; Olsbye, U.; Svelle, S. On How Copper Mordenite Properties Govern the Framework Stability and Activity in the Methane-to-Methanol Conversion. *ACS Catal.* **2018**, *9*, 365–375.
(32) Brezicki, G.; Kammert, J. D.; Gunnoe, T. B.; Paolucci, C.; Davis, R. J. Insights into the Speciation of Cu in the Cu-H-Mordenite Catalyst for the Oxidation of Methane to Methanol. *ACS Catal.* **2019**, *9*, 5308–5319.
(33) Pappas, D. K.; Borfecchia, E.; Dyballa, M.; Pankin, I. A.; Lomachenko, K. A.; Martini, A.; Signorile, M.; Teketel, S.; Arstad, B.; Berlier, G.; et al. Methane to Methanol: Structure-Activity Relationships for Cu-CHA. *J. Am. Chem. Soc.* **2017**, *139* (42), 14961–14975.
(34) Borfecchia, E.; Pappas, D. K.; Dyballa, M.; Lomachenko, K. A.; Negri, C.; Signorile, M.; Berlier, G. Evolution of Active Sites during Selective Oxidation of Methane to Methanol over Cu-CHA and Cu-MOR Zeolites as Monitored by Operando XAS. *Catal. Today* **2018**, No. in Press, https://doi.org/10.1016/j.cattod.2018.07.028.
(35) Li, H.; Paolucci, C.; Khurana, I.; Wilcox, L. N.; Göltl, F.; Albarracin-Caballero, J. D.; Shih, A. J.; Ribeiro, F. H.; Gounder, R.; Schneider, W. F. Consequences of Exchange-Site Heterogeneity and Dynamics on the UV-Visible Spectrum Of. *Chem. Sci.* **2019**, *10*, 2373–2384.
(36) Göltl, F.; Bulo, R. E.; Hafner, J.; Sautet, P. What Makes Copper-Exchanged SSZ-13 Zeolite Efficient at Cleaning Car Exhaust Gases? *J. Phys. Chem. Lett.* **2013**, *4*,

2244–2249.
(37) Göltl, F.; Müller, P.; Uchupalanun, P.; Sautet, P.; Hermans, I. Developing a Descriptor-Based Approach for CO and NO Adsorption Strength to Transition Metal Sites in Zeolites. *Chem. Mater.* **2017**, *29*, 6434–6444.
(38) Paolucci, C.; Parekh, A. A.; Khurana, I.; Di Iorio, J. R.; Li, H.; Albarracin Caballero, J. D.; Shih, A. J.; Anggara, T.; Delgass, W. N.; Miller, J. T.; et al. Catalysis in a Cage: Condition-Dependent Speciation and Dynamics of Exchanged Cu Cations in SSZ-13 Zeolites. *J. Am. Chem. Soc.* **2016**, *138* (18), 6028–6048.
(39) Göltl, F.; Love, A. M.; Hermans, I. Developing a Thermodynamic Model for the Interactions Between Water and Cu in the Zeolite SSZ-13. *J. Phys. Chem. C* **2017**, *121*, 6160–6169.
(40) Petitjean, H.; Chizallet, C.; Berthomieu, D. Modeling Ammonia and Water Co-Adsorption in Cu^{I}-SSZ-13 Zeolite Using DFT Calculations. *Ind. Eng. Chem. Res.* **2018**, *57* (47), 15982–15990.
(41) Xie, P.; Pu, T.; Aranovich, G.; Guo, J.; Donohue, M.; Kulkarni, A.; Wang, C. Bridging Adsorption Analytics and Catalytic Kinetics for Metal-Exchanged Zeolites. *Nat. Catal.* **2021**, *4*, 144–156.
(42) Palagin, D.; Knorpp, A.; B. P. Prieto, A.; Ranocchiari, M.; van Bokhoven, J. Assessing Relative Stability of Copper Oxide Clusters as Active Sites of CuMOR Zeolite for Methane to Methanol Conversion: Size Matters? *Nanoscale* **2016**, *9*, 1144–1153.
(43) Engedahl, U.; Grönbeck, H.; Hellman, A. First-Principles Study of Oxidation State and Coordination of Cu-Dimers in Cu-SSZ-13 during Methane-to-Methanol Reaction Conditions. *J. Phys. Chem. C* **2019**, *123* (43), 26145–26150.
(44) Paolucci, C.; Di Iorio, J. R.; Ribeiro, F. .; Gounder, R.; Schneider, W. F. Catalysis Science of NOx Selective Catalytic Reduction with Ammonia over Cu-SSZ-13 and Cu-SAPO-34. In *Advances in Catalysis*; Elsevier Inc., 2016; Vol. 59, pp 1–107.
(45) Beale, A. M.; Gao, F.; Lezcano-Gonzalez, I.; Peden, C. H. F.; Szanyi, J. Recent Advances in Automotive Catalysis for NO_x Emission Control by Small-Pore Microporous Materials. *Chem. Soc. Rev.* **2015**, *44*, 7371–7405.
(46) Göltl, F.; Love, A. M.; Schuenzel, S. C.; Wolf, P.; Mavrikakis, M.; Hermans, I. Computational Description of Key Spectroscopic Features of Zeolite SSZ-13. *Phys. Chem. Chem. Phys.* **2019**, *21*, 19065–19075.
(47) Loewenstein, W. The Distribution of Aluminum in the Tetrahedra of Silicates and Aluminates. *Am. Mineral.* **1954**, *39*, 92–96.
(48) Göltl, F.; Sautet, P.; Hermans, I. The Impact of Finite Temperature on the Coordination of Cu Cations in the Zeolite SSZ-13. *Catal. Today* **2016**, *267*, 41–46.
(49) Fickel, D. W.; Lobo, R. F. Copper Coordination in Cu-SSZ-13 and Cu-SSZ-16 Investigated by Variable-Temperature XRD. *J. Phys. Chem. C* **2010**, *114* (3), 1633–1640.
(50) Hun Kwak, J.; Zhu, H.; Lee, J. H.; Peden, C. H. F.; Szanyi, J. Two Different Cationic Positions in Cu-SSZ-13? *Chem. Commun. (Camb).* **2012**, *48* (39), 4758–4760.
(51) Deka, U.; Juhin, A.; Eilertsen, E. a; Emerich, H.; Green, M. a; Korhonen, S. T.; Weckhuysen, B. M.; Beale, A. M. Confirmation of Isolated Cu^{2+} Ions in SSZ-13 Zeolite as Active Sites in NH_3-Selective Catalytic Reduction. *J. Phys. Chem. C*

2012, *116* (7), 4809–4818.
(52) Sushkevich, V. L.; Palagin, D.; van Bokhoven, J. A. The Effect of the Active-Site Structure on the Activity of Copper Mordenite in the Aerobic and Anaerobic Conversion of Methane into Methanol. *Angew. Chemie - Int. Ed.* **2018**, *57* (29), 8906–8910.
(53) Knorpp, A. J.; Pinar, A. B.; Baerlocher, C.; McCusker, L. B.; Casati, N.; Newton, M. A.; Checchia, S.; Meyet, J.; Palagin, D.; van Bokhoven, J. A. Paired Copper Monomers in Zeolite Omega: The Active Site for Methane-to-Methanol Conversion. *Angew. Chemie - Int. Ed.* **2021**, *60* (11), 5854–5858.
(54) Perdew, J. P.; Burke, K.; Ernzerhof, M. Generalized Gradient Approximation Made Simple. *Phys. Rev. Lett.* **1996**, *77* (18), 3865–3868.
(55) Tkatchenko, A.; Scheffler, M. Accurate Molecular van Der Waals Interactions from Ground-State Electron Density and Free-Atom Reference Data. *Phys. Rev. Lett.* **2009**, *102* (7), 073005.
(56) Kresse, G.; Hafner, J. Ab Initio Molecular Dynamics for Open-Shell Transition Metals. *Phys. Rev. B* **1993**, *48* (17), 13115–13118.
(57) Kresse, G.; Furthmüller, J. Efficiency of Ab-Initio Total Energy Calculations for Metals and Semiconductors Using a Plane-Wave Basis Set. *Comput. Mater. Sci.* **1996**, *6* (1), 15–50.
(58) Göltl, F.; Hafner, J. Structure and Properties of Metal-Exchanged Zeolites Studied Using Gradient-Corrected and Hybrid Functionals . III . Energetics and Vibrational Spectroscopy of Adsorbates. *J. Chem. Phys.* **2012**, *136*, 064503.
(59) Marsman, M.; Grüneis, A.; Paier, J.; Kresse, G. Second-Order Møller-Plesset Perturbation Theory Applied to Extended Systems. I. Within the Projector-Augmented-Wave Formalism Using a Plane Wave Basis Set. *J. Chem. Phys.* **2009**, *130* (18), 1–10.
(60) Harl, J.; Kresse, G. Cohesive Energy Curves for Noble Gas Solids Calculated by Adiabatic Connection Fluctuation-Dissipation Theory. *Phys. Rev. B - Condens. Matter Mater. Phys.* **2008**, *77* (4), 1–8.
(61) Tuma, C.; Kerber, T.; Sauer, J. The Tert-Butyl Cation in h-Zeolites: Deprotonation to Isobutene and Conversion into Surface Alkoxides. *Angew. Chemie - Int. Ed.* **2010**, *49* (27), 4678–4680.
(62) Göltl, F.; Michel, C.; Andrikopoulos, P. C.; Love, A. M.; Hafner, J.; Hermans, I.; Sautet, P. Computationally Exploring Confinement Effects in the Methane-to-Methanol Conversion Over Iron-Oxo Centers in Zeolites. *ACS Catal.* **2016**, *6*, 8404–8409.
(63) Göltl, F.; Hafner, J. Alkane Adsorption in Na-Exchanged Chabazite: The Influence of Dispersion Forces. *J. Chem. Phys.* **2011**, *134* (6), 064102.
(64) Göltl, F.; Grüneis, A.; Bučko, T.; Hafner, J. Van Der Waals Interactions between Hydrocarbon Molecules and Zeolites: Periodic Calculations at Different Levels of Theory, from Density Functional Theory to the Random Phase Approximation and Moller-Plesset Perturbation Theory. *J. Chem. Phys.* **2012**, *137* (11), 114111.
(65) Göltl, F.; Sautet, P.; Hermans, I. Can Dynamics Be Responsible for the Complex Multipeak Infrared Spectra of NO Adsorbed to Copper(II) Sites in Zeolites? *Angew. Chemie - Int. Ed.* **2015**, *54* (27), 7799–7804.
(66) Di Iorio, J. R.; Gounder, R. Controlling the Isolation and Pairing of Aluminum in

Chabazite Zeolites Using Mixtures of Organic and Inorganic Structure-Directing Agents. *Chem. Mater.* **2016**, *28*, 2236–2247.
(67) Blöchl, P. E. Projector Augmented-Wave Method. *Phys. Rev. B* **1994**, *50* (24), 17953–17979.
(68) Kresse, G.; Joubert, D. From Ultrasoft Pseudopotentials to the Projector Augmented-Wave Method. *Phys. Rev. B* **1999**, *59* (3), 1758–1775.
(69) Göltl, F.; Hafner, J. Structure and Properties of Metal-Exchanged Zeolites Studied Using Gradient-Corrected and Hybrid Functionals. I. Structure and Energetics. *J. Chem. Phys.* **2012**, *136* (6), 064501.
(70) Andersen, H. C. Molecular Dynamics Simulations at Constant Pressure and / or Temperature. *J. Chem. Phys.* **1980**, *72*, 2384.
(71) Irikura, K. K. Thermo.Pl. *Natl. Inst. Stand. Technol.* **2002**.
(72) Kulkarni, A. R.; Zhao, Z. J.; Siahrostami, S.; Nørskov, J. K.; Studt, F. Monocopper Active Site for Partial Methane Oxidation in Cu-Exchanged 8MR Zeolites. *ACS Catal.* **2016**, *6* (10), 6531–6536.
(73) Pappas, D. K.; Borfecchia, E.; Dyballa, M.; Pankin, I.; Lomachenko, K. A.; Martini, A.; Signorile, M.; Teketel, S.; Arstad, B.; Berlier, G.; et al. Methane to Methanol: Structure-Activity Relationships for Cu-CHA. *J. Am. Chem. Soc.* **2017**, *139*, 14961–14975.
(74) Shaik, S.; Cohen, S.; de Visser, S. P.; Sharma, P. K.; Kumar, D.; Kozuch, S.; Ogliaro, G.; Danovich, D. The ‘“ Rebound Controversy ”’: An Overview and Theoretical Modeling of the Rebound Step in C-H Hydroxylation by Cytochrome P450. *Eur. J. Inorg. Chem.* **2004**, 207–226.
(75) Ye, S.; Geng, C.-Y.; Shaik, S.; Neese, F. Electronic Structure Analysis of Multistate Reactivity in Transition Metal Catalyzed Reactions: The Case of C-H Bond Activation by Non-Heme Iron(IV)-Oxo Cores. *Phys. Chem. Chem. Phys.* **2013**, *15*, 8017.
(76) Yoshizawa, K.; Shiota, Y.; Yamabe, T. Abstraction of the Hydrogen Atom of Methane by Iron−Oxo Species: The Concerted Reaction Path Is Energetically More Favorable. *Organometallics* **1998**, *17* (13), 2825–2831.